ANGULAR MOMENTUM DENSITY OF SURFACE PLASMON POLARITON ENHANCED ELECTROMAGNETIC FIELDS EXCITED BY TIGHTLY FOCUSED STATISTICAL BEAMS

by

Hao Cheng

Submitted in partial fulfillment of the
requirements for the degree of
Master of Applied Science

at

Dalhousie University
Halifax, Nova Scotia
April 2015

To my parents

Table of Contents

List of Figures . . . . **v**

Abstract . . . . **vi**

List of Symbols Used . . . . **vii**

Acknowledgements . . . . **viii**

Chapter 1 Introduction **1**

1.1 Background 1

1.2 Motivation and Objectives 2

1.3 Thesis Contributions 2

1.4 Thesis Organization 3

Chapter 2 Background Information **4**

2.1 Introduction to Surface Plasmon Polaritons 4
  2.1.1 Surface Plasmon Polariton Properties 4
  2.1.2 Excitation of Surface Plasmon Polaritons 5

2.2 Angular spectrum representation of optical fields 7
  2.2.1 Introduction 7
  2.2.2 Far-fields in the Angular Spectrum Representation 9

2.3 Coherent-mode representation 10
  2.3.1 Introduction to Coherence Theory 10
  2.3.2 Coherent-Mode Representation of Twisted Gaussian Schell-model Beams 11

Chapter 3 Angular Momentum Density of Surface Plasmon Enhanced Electromagnetic Fields Excited by Tightly Focused Statistical Beams **13**

3.1 Theory 13

3.2 Results 25

Chapter 4 Conclusions and Future Work **30**

4.1 Conclusions 30

4.2 Recommendations for future work 30

Bibliography **32**

Appendix A Modal Weights in the Maximal Twist and No Twist Cases 36

Appendix B Numerical Codes for Solving Spectral Density **39**

Appendix C Numerical Codes for Solving Angular Momentum Density **42**

List of Figures

Figure 2.1 Dispersion relation at a gold-air interface. The solid line shows the dispersion relation of SPPs derived from Eq.(2.1). The two dash-dotted straight lines represent the free-space light line $\omega = ck_x$ and the tilted light line in glass $\omega = ck_x/n$, respectively. . 5

Figure 2.2 Experimental configurations to realize SPP excitation (a)Otto configuration. (b)Kretschmann configuration.L: laser, D: detector, M: metal layer. 6

Figure 2.3 The optical scattering problem expressed in the angular spectrum representation. 7

Figure 3.1 Illustrating SPP generation by tight focusing. 13

Figure 3.2 The relationship between s-polarization and p-polarization. . . 14

Figure 3.3 Geometrical representation of the focusing process. 15

Figure 3.4 Optical intensity in the glass-silver-air configuration. 25

Figure 3.5 Optical intensity in the glass-air configuration. 26

Figure 3.6 Azimuthal component of the averaged angular momentum density in no twist condition with (a)$\sigma_c = 10^5\sigma_I$, (b)$\sigma_c = \sigma_I$, (c)$\sigma_c = 0.5\sigma_I$. 27

Figure 3.7 Axial component of the angular momentum density with $u\sigma_c^2 = 1$ and coherence length $\sigma_c = 0.5\sigma_I$. 28

Figure 3.8 Axial component of the angular momentum density with $u = 0$ and coherence length $\sigma_c = 0.5\sigma_I$. 28

Figure 3.9 Configuration of a holographic optical trapping system 29

Abstract

Our work in plasmonics is concerned with coherence properties of partially coherent, twisted Gaussian-Schell model (TGSM) beams tightly focused on a thin metal film. We have simulated the spectral density of in-coupled light and shown that it is strongly affected by the surface plasmon polariton (SPP) generation. This also confirms our original assumption that strong SPP coupling can be realized in this configuration. The calculation of the angular momentum density shows that its distribution can be controlled by the beam coherence length and a twist parameter magnitude. The sharp angular momentum density maxima and their distribution tend to be smeared out as the coherence length decreases. In addition, the axial component of angular momentum distribution becomes delocalized as the strength of phase twist of an incident beam is increased.

List of Symbols Used

$\mathbf{E}$	Electrical Field
$\mathbf{H}$	Magnetic Field
$\mathbf{S}$	Poynting Vector
$\mathbf{L}$	Angular Momentum Density
$\mathbf{E}_{inc}$	Incident Electrical Field
$\mathbf{E}_t$	Transmitted Field
$\mathbf{E}_\infty$	Far-field Near Spherical Surface
$\mathbf{E}_\infty^t$	Far-field of Transmitted Field
ε_0	Free Space Permittivity
μ_0	Free Space Permeability
$Z_{\mu\varepsilon}$	Wave Impedance
k_{spp}	Wavenumber of SPP
θ_{spp}	SPP-resonance Angle
c	Speed of Light
n	Refractive Index
ω	Angular Frequency
λ	Wavelength in Free Space
ρ	Position Vector
f	Focal Length
σ_c	Coherence Length
σ_I	Beam Width
W_{TGSM}	Cross-spectra Density of TGSM
$\ell_\perp$	Characteristic Width of Mode
$\widetilde{T}_{13}$	Fresnel Transmission Coefficient

Acknowledgements

This thesis would not have been possible without the support of many people. Many thanks to my supervisor, Dr. Sergey Ponomarenko, who gives me not only proper and timely guidance, but also lots of encouragement during the research. I should also thank my committee members, Dr. Zhizhang Chen and Dr. William J. Phillips, who offered me guidance and support. Their insightful comments are really helpful to the thesis. In addition, I am thankful to my colleagues, especially Shunchuan Yang for providing lots of help during my research. Finally, I should appreciate my parents. It would be impossible to finish this thesis without their help.

Chapter 1

Introduction

1.1 Background

In the 19th century, the existence of electromagnetic waves was suggested by James Clerk Maxwell [1]. He worked out mathematically the properties they might have, after having collected and summarized research achievements in the field of electromagnetism by other researchers. Thus, the classical electromagnetic theory was established. At the same time, Maxwell related optical phenomena to electromagnetic phenomena, having pointed out that light was an electromagnetic wave, thereby building the electromagnetic theory of optics. This achievement made a great contribution to the development of physics. The electromagnetic waves play an essential role in our life, not only in the field of engineering, but also in various other fields like medicine [2], space exploration [3] and communications [4], to name but a few. Plasmonics is a branch of science connecting research on electromagnetic fields and on free electrons in metals [5].

Research in plasmonics, which forms a major part of the fascinating field of nanophotonics, has been growing rapidly since the first decade of the twenty-first century [6]. It offers us new perspectives to explore the properties of electromagnetic fields over dimensions smaller than the wavelength of light [7]. The light energy can be tightly confined to metal-dielectric interfaces by plasmons. Hence, strong electromagnetic fields can be generated in a vicinity of metal/dielectric interfaces [8]. To date, plasmonics effects have been applied to a wide range of fields, including nanoscale waveguides [9], high-resolution microscopy [10], sensors [11], and nonlinear optics [12].

1.2 Motivation and Objectives

The surface plasmon resonance can be supported at an interface between two materials where the real part of the dielectric function changes sign across the interface [13], such as silver and air. Coherent oscillations of the surface conduction electrons will be produced at the carrier frequency of a driving electromagnetic wave [14]. However, a lot of researches in plasmonics deal with only deterministic situations [15, 16]. That means the physical quantities are expressed by mathematical functions that are either fully specified or are predicted to be precisely measurable. The conclusions drawn from deterministic and statistical analyses of the same realistic problem can differ greatly [17]. That is the reason we employ statistical models in our research to obtain simulation results corresponding to realistic laboratory conditions of noisy light sources. The objective of this thesis is to control the field energy and angular momentum distributions by adjusting spatial coherence properties of the incident light.

1.3 Thesis Contributions

This thesis is concerned with the energy and angular momentum distributions of statistical light beams tightly focused on a thin metal film. We have made the following contributions :

- We apply statistical analyses to explore the properties of transmitted beams near the metal film. The obtained theoretical results correspond to realistic situation of the film illuminated by a noisy light source.

- We have simulated the spectra of transmitted light in the Kretschmann and glass-air configurations. Our results indicate that transmitted electromagnetic fields are strongly affected by the surface plasmon polariton (SPP) generation. The results prove our original assumption that strong plasmon coupling can be realized in the Kretschmann configuration.

- It has been demonstrated in the reference that coherence of the incident light is controlled by both the beam width and a twist parameter [18].Our simulated results prove that coherence also affects the energy distribution of the SPP-enhanced light fields.

- We simulated the angular momentum density of the SPP-enhanced transmitted field in cases of no twist and maximal twist of the incident beam phase. The results show that we can control the distribution and periodicity of the angular momentum density by changing the strength of the twist parameter.

1.4 Thesis Organization

The thesis is organized as follows. Chapter 2 starts out by providing an overview of the theoretical foundations and background information—including introductions to SPPs, coherence theory, and the principles of coherent-mode representation. Chapter 3 proceeds with the problem formulation, theoretical description, numerical modelling and discussion of results. Finally, conclusions are presented in chapter 4.

Chapter 2

Background Information

2.1 Introduction to Surface Plasmon Polaritons

The prediction of the existence of surface plasmon polaritons (SPP) was first presented by Rufus Ritchie in 1957 [19]. SPPs represent surface charge density oscillations sustained by metal's free electron gas at optical frequencies. Similar behavior cannot be simply realized in other spectral ranges because metal parameters change considerably with the electromagnetic wave carrier frequency. The SPPs excited at the interface between a metal, possessing a negative dielectric permittivity, and a dielectric can produce strongly enhanced optical near fields which propagate along the metal surface.

2.1.1 Surface Plasmon Polariton Properties

It is sometimes stated that SPPs are quanta of surface charge density oscillations [13]. SPPs can also be viewed as collective oscillations of the electron density at the surface of a metal. The SPPs are naturally coupled to carrier waves at optical frequencies. Solving the Maxwell equations with the appropriate boundary conditions in the media gives us a dispersion relation for SPPs as [13]

$$k_{spp} = \frac{\omega}{c}\sqrt{\frac{\varepsilon_m \varepsilon_d}{\varepsilon_m + \varepsilon_d}}. \tag{2.1}$$

Here ε_m denotes the complex dielectric permittivity of a noble metal that depends on the frequency of light, with a negative real part, and ε_d stands for a positive real dielectric constant of a dielectric material. To discuss some properties of SPPs, the imaginary part of ε_m needs to be specified. Assume that $\varepsilon_m = \varepsilon'_m + i\varepsilon''_m$ and $k_{spp} = k'_{spp} + ik''_{spp}$ with constraints that $\varepsilon'_m < 0$ and $|\varepsilon'_m| >> \varepsilon''_m$. It follows that k_{spp} can be determined as [13]

$$k'_{spp} = \frac{\omega}{c}\sqrt{\frac{\varepsilon'_m \varepsilon_d}{\varepsilon'_m + \varepsilon_d}}, \tag{2.2}$$

and

$$k''_{spp} \simeq \frac{\omega}{c}\sqrt{\frac{\varepsilon'_m \varepsilon_d}{\varepsilon'_m + \varepsilon_d}} \frac{\varepsilon''_m \varepsilon_d}{2\varepsilon'_m(\varepsilon'_m + \varepsilon_d)}. \tag{2.3}$$

The SPP wavelength is determined by the real part k'_{spp}, such that

$$\lambda_{spp} = \frac{2\pi}{k'_{spp}} \approx \sqrt{\frac{\varepsilon'_m + \varepsilon_d}{\varepsilon'_m \varepsilon_d}}\lambda. \tag{2.4}$$

where λ represents the wavelength of the excitation light in vacuum.

On the other hand, the propagation length of SPPs along the interface is determined by k''_{spp}, which is responsible for an exponential decay of the electric field amplitude, since the SPP energy is lost to ohmic resistance and is deposited in the form of heat. The 1/e decay length of the electric field equals to $1/k''_{spp}$ or $1/(2k''_{spp})$ for the intensity. After comparing the 1/e decay lengths of SPPs on both sides of the interface, it can be concluded that the decay length into the metal is much shorter than into the dielectric.

2.1.2 Excitation of Surface Plasmon Polaritons

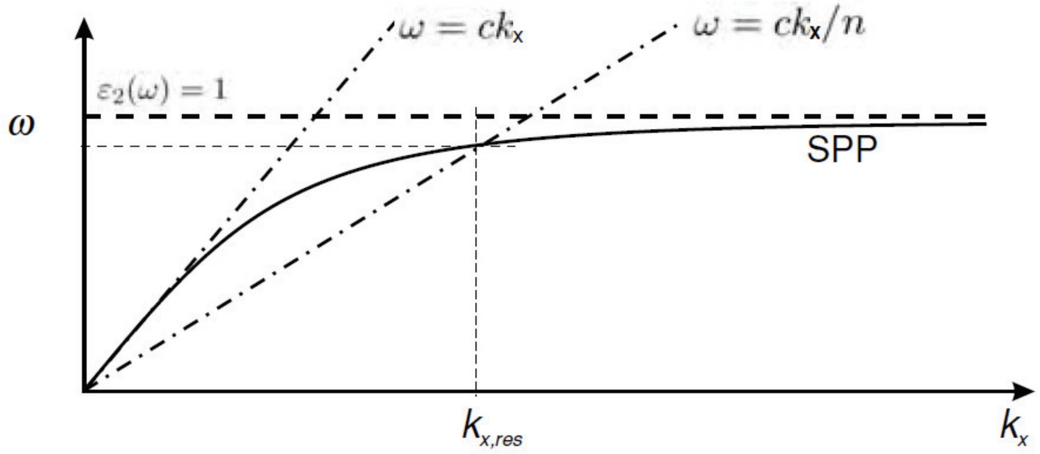

Figure 2.1: Dispersion relation at a gold/air interface. The solid line shows the dispersion relation of SPPs derived from Eq.(2.1). The two dash-dotted straight lines represent the free-space light line $\omega = ck_x$ and the tilted light line in glass $\omega = ck_x/n$, respectively(Figure source: Fig 12.6(a), pp.389, [13]).

To excite SPPs, optical beam coupling with the SPP frequency is required. The

SPPs can only be generated by fulfilling both energy and momentum conservation conditions. Fig 2.1 exhibits an SPP dispersion relation.

We can see that for a given frequency ω, the wavenumber k'_{spp} is always greater than the wavenumber of light in free space. The physical reason for this is the light field has to drag electrons along the metal surface. Thus, light propagating in the air cannot excite SPPs at a metal-air interface. In other words, the SPP dispersion curve does not intersect the photon dispersion curve in the air. Consequently, we need to increase the in-plane wave vector component of the SPP exciting light over its value in the air. To this end, one can use evanescent waves created by a medium with a refractive index $n > 1$, such as glass, to excite SPPs. The dispersion curve of an example of such a wave is displayed in Fig 2.1, which is tilted by a factor of n since $\omega = ck/n$. There are two possible experimental configurations that fulfill our requirements, both shown in Fig 2.2.

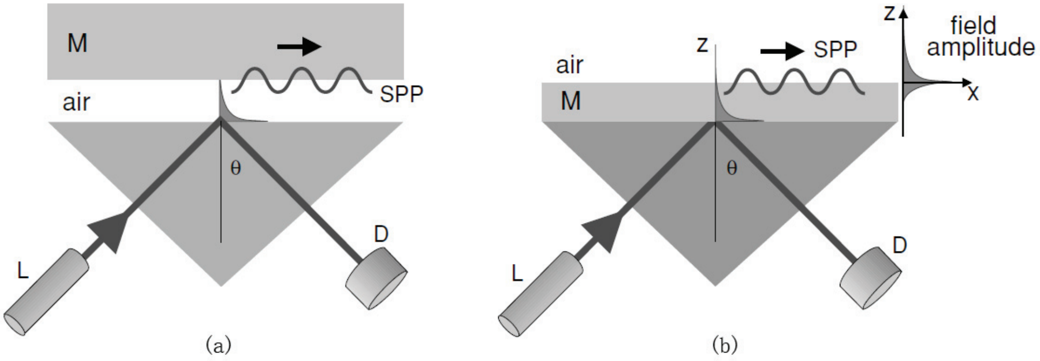

Figure 2.2: Experimental configurations to realize SPP excitation (a)Otto configuration. (b)Kretschmann configuration.L: laser, D: detector, M: metal layer(Figure source: Fig 12.6(b), pp.389, [13]).

In the Otto configuration, the SPPs are excited by the tail of an evanescent wave coming out of the glass-air interface. However, this configuration is not experimentally viable because it is hard to control the width of the tiny gap between the two interfaces. That is the reason we apply an alternative, Kretschmann configuration in our numerical simulations. In the Kretschmann configuration, a thin metal film is deposited on top of the glass prism. The film thickness can be conveniently controlled. The SPPs can be excited by the evanescent wave penetrating through the metal film with a proper thickness.

2.2 Angular spectrum representation of optical fields

2.2.1 Introduction

The angular spectrum representation is a powerful mathematical technique to describe laser beam propagation and light focusing as a superposition of plane and evanescent waves of different directions calculated from Maxwell's equations [13], which can then be individually propagated through an optical system of interest. A plane wave is a wave that propagates in one direction. The wavefronts of plane waves are perpendicular to the direction of propagation and have the same value [20]. An evanescent wave does not propagate but rather decays exponentially with distance [21].

If the angular spectrum representation is treated in the paraxial limit, it can be regarded as the framework of Fourier optics, which finds numerous applications such as spatial filtering [13], optical correlations [13] and computer generated holograms [22]. Let $\mathbf{E}(\mathbf{r})$ to be an electric field at a certain point $\mathbf{r} = (x, y, z)$ in space.

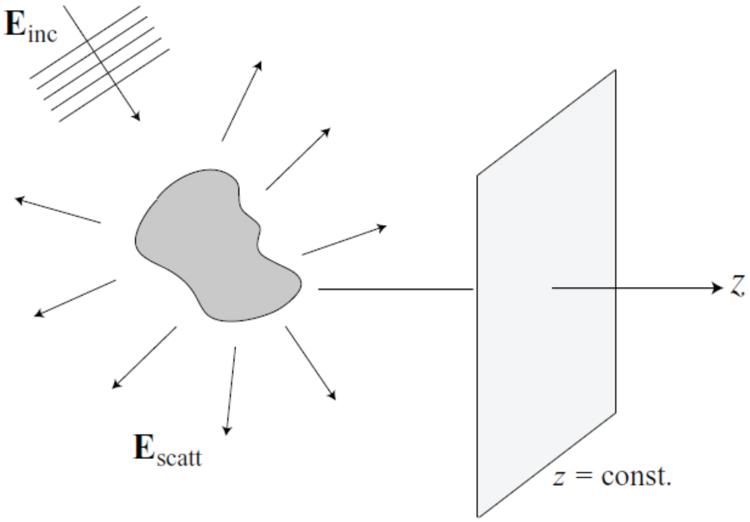

Figure 2.3: The optical scattering problem expressed in the angular spectrum representation(Figure source: Fig 2.9, pp.39, [13]).

In Fig 2.3 we sketch a typical scattering problem. One can choose an arbitrary axis z and consider the field $\mathbf{E}$ in a plane $z = const$. The field $\mathbf{E}$ at any point in space can be determined by combining the contributions of each plane wave since the propagation characteristics of plane waves in free space are well known [23]. A two-dimensional Fourier transform of the field $\mathbf{E}$ is defined as [13]

$$\hat{\mathbf{E}}(k_x, k_y; z) = \frac{1}{4\pi^2} \iint_{-\infty}^{\infty} \mathbf{E}(x, y, z) e^{-i(k_x x + k_y y)} dx dy. \tag{2.5}$$

Similarly, we express the inverse Fourier transform as

$$\mathbf{E}(x, y, z) = \iint_{-\infty}^{\infty} \hat{\mathbf{E}}(k_x, k_y; z) e^{i(k_x x + k_y y)} dk_x dk_y. \tag{2.6}$$

Here x, y are the Cartesian coordinates in a plane transverse to the z-axis and k_x, k_y are the corresponding spatial frequencies. If the medium is confined to be homogeneous, isotropic, linear and source-free, the electric field has to satisfy the vector Helmholtz equation in the form

$$(\bigtriangledown^2 + k^2)\mathbf{E}(\mathbf{r}) = 0. \tag{2.7}$$

Here $k = (\omega/c)n$. In the space-time domain the electric field can be written as

$$\mathbf{E}(\mathbf{r}, t) = Re[\mathbf{E}(\mathbf{r})e^{-i\omega t}]. \tag{2.8}$$

Substituting from (2.6) into (2.7), we obtain the expression

$$\hat{\mathbf{E}}(k_x, k_y; z) = \hat{\mathbf{E}}(k_x, k_y; 0)e^{\pm i k_z z}, \tag{2.9}$$

where

$$k_z = \begin{cases} \sqrt{k^2 - k_x^2 - k_y^2}, & k_x^2 + k_y^2 \leq k^2, \quad \text{homogeneous waves;} \\ i\sqrt{k_x^2 + k_y^2 - k^2}, & k_x^2 + k_y^2 > k^2, \quad \text{evanescent waves.} \end{cases} \tag{2.10}$$

The wavenumber k_z is either real or imaginary and turns the factor $\exp(\pm i k_z z)$ into an oscillatory or exponentially decaying function, which determines the type of wave. It follows from (2.6) and (2.9), that the electric field at an arbitrary position can be represented as

$$\mathbf{E}(x, y, z) = \iint_{-\infty}^{\infty} \hat{\mathbf{E}}(k_x, k_y; 0) e^{i(k_x x + k_y y \pm k_z z)} dk_x dk_y. \tag{2.11}$$

Eq.(2.11) is known as the angular spectrum representation [13]. There is one more aspect we should mention. Although the angular spectrum of **E** fulfills the Helmholtz equation, it is not yet a rigorous solution of Maxwell's equations in free space. It is necessary to require that the fields be divergence free, i.e. $\nabla \cdot \mathbf{E} = 0$. The condition confines $\mathbf{k}$ to directions perpendicular to the spectral amplitudes.

2.2.2 Far-fields in the Angular Spectrum Representation

With the use of angular spectrum representation, a rigorous description of near fields can be realized in terms of the corresponding far fields, which are conveniently determined. Eq.(2.11) describes field propagation from the source $z = 0$ to any plane $z = const$. The dimensionless unit vector $\mathbf{s}$ in the direction of $\mathbf{r}$ can be expressed as [13]

$$\mathbf{s} = (s_x, s_y, s_z) = \left(\frac{x}{r}, \frac{y}{r}, \frac{z}{r}\right), \tag{2.12}$$

where $r = (x^2 + y^2 + z^2)^{\frac{1}{2}}$ is the distance from the origin. Eq.(2.11) can then be transformed to

$$\mathbf{E}_\infty(s_x, s_y, s_z) = \lim_{kr\to\infty} \iint_{(k_x^2+k_y^2)\leq k^2} \hat{\mathbf{E}}(k_x, k_y; 0) e^{ikr[\frac{k_x}{k}s_x + \frac{k_y}{k}s_y \pm \frac{k_z}{k}s_z]} dk_x dk_y. \tag{2.13}$$

The integration range is confined to $(k_x^2 + k_y^2) \leq k^2$ due to the exponential decay of the evanescent waves. Eq.(2.13) can be expressed as [24]

$$\mathbf{E}_\infty(s_x, s_y, s_z) = -2\pi i k s_z \hat{\mathbf{E}}(ks_x, ks_y; 0) \frac{e^{ikr}}{r}. \tag{2.14}$$

It follows from Eq.(2.14) that the far-fields are entirely determined by the Fourier spectra of the fields $\hat{\mathbf{E}}(ks_x, ks_y; 0)$ in the source plane if we replace k_x and k_y by ks_x and ks_y. This simply means that $\mathbf{s}$ fulfills the condition

$$\mathbf{s} = (s_x, s_y, s_z) = \left(\frac{k_x}{k}, \frac{k_y}{k}, \frac{k_z}{k}\right). \tag{2.15}$$

The result implies that due to destructive interference, only one plane wave with the wavevector $\mathbf{k} = (k_x, k_y, k_z)$ at $z = 0$ contributes to the far-field in the direction $\mathbf{s}$. Thus we can treat the far-fields as a collection of rays with each ray being characterized by a particular plane wave. On substituting from (2.15) into (2.14), the Fourier spectrum of $\hat{\mathbf{E}}$ is found to be given by

$$\hat{\mathbf{E}}(k_x, k_y; 0) = \frac{ire^{-ikr}}{2\pi k_z} \mathbf{E}_\infty(k_x, k_y). \tag{2.16}$$

Eq.(2.16) can be substituted into (2.11) yielding

$$\mathbf{E}(x,y,z)=\frac{ire^{-ikr}}{2\pi}\iint_{(k_x^2+k_y^2)\leq k^2}\mathbf{E}_\infty(k_x,k_y)e^{i(k_xx+k_yy\pm k_zz)}\frac{1}{k_z}dk_xdk_y. \tag{2.17}$$

Eq.(2.17) is a rigorous expression of near-field angular distributions in terms of far fields [13].

2.3 Coherent-mode representation

2.3.1 Introduction to Coherence Theory

Coherence theory describes correlations among physical properties of a single wave, or several waves. There are two types of coherence, temporal coherence and spatial coherence [17]. Assume $V(\mathbf{r},t)$ to be an optical field at a point specified by the position vector $\mathbf{r}$ and at time t. $V(\mathbf{r},t)$ is a fluctuating function of space and time for any realistic optical field. The random field is stationary in the wide sense if its cross-correlation function depends only on the difference between two time arguments $\tau=t_2-t_1$, expressed as [25]

$$\Gamma(\mathbf{r_1},\mathbf{r_2},\tau)=\langle V^*(\mathbf{r_1},t)V(\mathbf{r_2},t+\tau)\rangle. \tag{2.18}$$

Here angle brackets denote averaging over a field ensemble $\{V\}$. Eq. (2.18) is known as the mutual coherence function and describes a statistical optical field in the space-time domain. Assuming that $\Gamma(\mathbf{r_1},\mathbf{r_2},\tau)$ is absolutely integrable in the range $-\infty<\tau<\infty$, it can be represented by its Fourier transform as

$$W(\mathbf{r_1},\mathbf{r_2},\omega)=\int_{-\infty}^{\infty}\Gamma(\mathbf{r_1},\mathbf{r_2},\tau)exp(-i\omega\tau)d\tau, \tag{2.19}$$

which is known as the cross-spectral density function of the field and is a central quantity of the second-order coherence theory in the space-frequency domain [25].

The cross-spectral density function becomes the spectral density if $\mathbf{r_1}=\mathbf{r_2}=\mathbf{r}$, which can be expressed as

$$S(\mathbf{r},\omega)=W(\mathbf{r},\mathbf{r},\omega). \tag{2.20}$$

It can be shown that [17]

$$|W(\mathbf{r_1},\mathbf{r_2},\omega)|\leq[S(\mathbf{r_1},\omega)]^{1/2}[S(\mathbf{r_2},\omega)]^{1/2}. \tag{2.21}$$

Thus the normalized cross-spectral density function can be defined as

$$\mu(\mathbf{r_1}, \mathbf{r_2}, \omega) = \frac{W(\mathbf{r_1}, \mathbf{r_2}, \omega)}{[S(\mathbf{r_1}, \omega)]^{1/2}[S(\mathbf{r_2}, \omega)]^{1/2}}, \tag{2.22}$$

known as the spectral degree of coherence. The magnitude of the spectral degree of coherence satisfies the inequality [17]

$$0 \leq |\mu(\mathbf{r_1}, \mathbf{r_2}, \omega)| \leq 1. \tag{2.23}$$

If $|\mu| = 0$ for each pair of $\mathbf{r_1}$ and $\mathbf{r_2}$, the field is completely incoherent; when $|\mu| = 1$, it is completely coherent; and when $0 < |\mu| < 1$, it is partially coherent in space.

2.3.2 Coherent-Mode Representation of Twisted Gaussian Schell-model Beams

According to the theory advanced by E.Wolf in the 1980s, statistically stationary optical fields with arbitrary coherence can be expressed as a superposition of coherent modes in the space-frequency domain, which gives us a new insight into the physics of generation, propagation, and transformation of optical fields. If the cross-spectral density $W(\boldsymbol{\rho}_1, \boldsymbol{\rho}_2, \omega)$ is a continuous function, it can be expressed in the form of Mercer's expansion as [25]

$$W(\boldsymbol{\rho}_1, \boldsymbol{\rho}_2, \omega) = \sum_n \lambda_n(\omega)\psi_n^*(\boldsymbol{\rho}_1, \omega)\psi_n(\boldsymbol{\rho}_2, \omega), \tag{2.24}$$

where $\{\lambda_n(\omega)\}$ and $\{\psi_n(\boldsymbol{\rho}, \omega)\}$ are obtained by solving the integral equation as

$$\int W(\boldsymbol{\rho}_1, \boldsymbol{\rho}_2, \omega)\psi_n(\boldsymbol{\rho}_1, \omega)d\boldsymbol{\rho}_1 = \lambda_n(\omega)\psi_n(\boldsymbol{\rho}_2, \omega). \tag{2.25}$$

It is necessary to highlight that all the eigenvalues $\{\lambda_n(\omega)\}$ are real and nonnegative, such that

$$\lambda_n^*(\omega) = \lambda_n(\omega) \geq 0, \tag{2.26}$$

and the eigenfunctions $\{\psi_n(\boldsymbol{\rho}, \omega)\}$ are mutually orthonormal, such that

$$\int \psi_n^*(\boldsymbol{\rho}, \omega)\psi_m(\boldsymbol{\rho}, \omega)d\boldsymbol{\rho} = \delta_{nm}, \tag{2.27}$$

where δ_{nm} is the Kronecker symbol.

The Gaussian Schell-model (GSM) sources have shown great promise in optical coherence theory [12] since they model generic properties of many realistic partially coherent sources. GSM have been widely used, either for exploring the relationship between radiometry and coherence [26] or introducing the concept of twist phase for partially coherent beams [27]. In our simulations, we employ the twisted Gaussian Schell-model (TGSM) beams which carry a position-dependent twist phase. Here the twist factor presence offers an opportunity to control coherence without affecting the beam intensity profile [18]. TGSM beams have found numerous applications, including the theory of partially coherent solitons [18] and a ghost imaging technique [28]. The expression for the cross-spectral density of a TGSM beam W_{TGSM} is

$$W_{TGSM}(\boldsymbol{\rho}_1, \boldsymbol{\rho}_2) \propto \exp\left(-\frac{\rho_1^2 + \rho_2^2}{4\sigma_I^2}\right) \exp\left[-\frac{(\boldsymbol{\rho}_1 - \boldsymbol{\rho}_2)^2}{2\sigma_c^2}\right] \exp\left[iu\rho_1\rho_2 \sin(\phi_1 - \phi_2)\right]. \tag{2.28}$$

Here σ_I and σ_c represent the beam width and the spatial coherence length, respectively, and u is known as the twist parameter. The coherent-mode representation of the cross-spectral density of TGSM was derived in Ref[18]:

$$W_{TGSM}(\boldsymbol{\rho}_1, \boldsymbol{\rho}_2) = \sum_{m=-\infty}^{\infty} \sum_{n=0}^{\infty} \lambda_{mn} \psi_{mn}^*(\rho_1, \phi_1) \psi_{mn}(\rho_2, \phi_2), \tag{2.29}$$

where

$$\lambda_{mn} = \frac{n!}{n + |m|!} \zeta^{n + \frac{|m|}{2}} \eta^m, \tag{2.30}$$

and

$$\psi_{mn}(\rho, \phi) = \left(\frac{\rho}{\ell_\perp}\right)^{|m|} L_n^{|m|}\left(\frac{\rho^2}{{\ell_\perp}^2}\right) e^{-\frac{\rho^2}{2{\ell_\perp}^2}} e^{im\varphi}. \tag{2.31}$$

Here $\ell_\perp$ denotes a characteristic width of each mode in the transverse plane, given by

$$\ell_\perp = \sqrt{\frac{2\sigma_c^2 \sigma_I^2 (1 + \zeta)}{(2\sigma_I^2 + \sigma_c^2)(1 - \zeta)}}, \tag{2.32}$$

and the derivations of η and ζ are shown in Chapter 3.

The TGSM is treated as the incident source in our simulations. The coherent-mode representation of TGSM beams greatly simplifies the calculation of focusing integrals in Chapter 3.

Chapter 3

Angular Momentum Density of Surface Plasmon Enhanced Electromagnetic Fields Excited by Tightly Focused Statistical Beams

3.1 Theory

Tightly focused laser beams are used in fluorescence spectroscopy to study molecular interactions in solutions, as well as kinetics of single molecules at the interfaces [29]. They also show great promise in confocal microscopy [30] and optical data storage [31]. Furthermore, focused laser beams can be employed to trap nanoparticles and to move them with high precision [32].

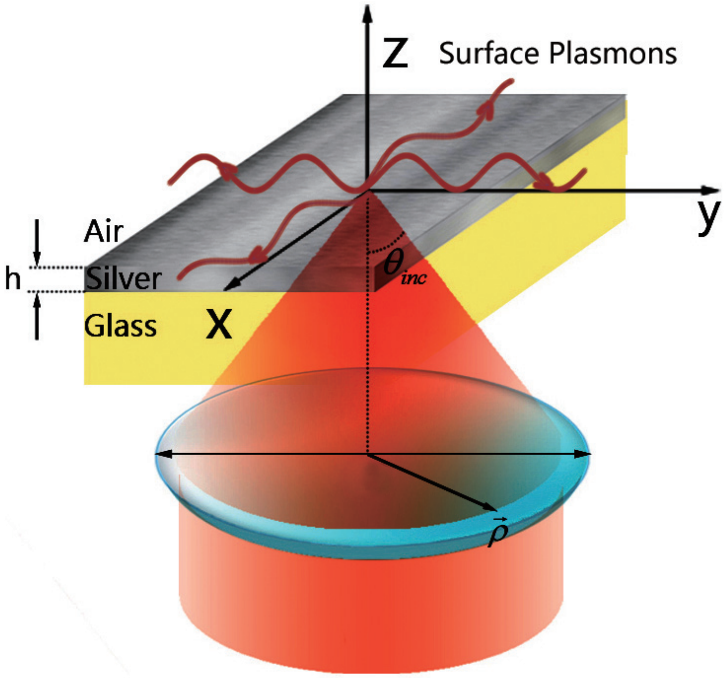

Figure 3.1: Illustrating SPP generation by tight focusing.

Investigations on optical manipulation of neutral nanoparticles have been extended to the control of optical torque and optical angular momentum [33]. It has been shown that light carries both spin angular momentum and orbital angular momentum, which can be used to rotate small particles [34]. Thus light has been applied to the optical tweezer technology, which uses highly focused laser beams to provide an attractive or repulsive force to physically move or rotate nanoparticles similar to tweezers [32]. The coherence properties of the light source play an important role in the simulation results. As a matter of fact, realistic light sources are necessarily partially spatially coherent to some extent. In addition, decreasing the spatial coherence of light source generally reduces the interference signal produced by multiply scattered light , while increasing the spatial coherence guarantees of undamped signal strength in a large axial imaging range [35]. In this thesis, we use incident beams that are partially spatially coherent. On the other hand, dielectric nanoparticles respond rather weakly to applied optical fields necessitating the use of very tight optical traps. To mitigate this circumstance, SPPs have been widely used to enhance the optical response of sub-wavelength particles [36]. Plasmonics encompasses SPP studies and nano-optics and it has found numerous applications ranging from merging photonics and electronics at nanoscale dimensions [37] to cancer treatment [38].

In our thesis, SPPs are excited at an Ag-air interface by localized fields originating from TGSM laser beams, which are tightly focused by a large numerical aperture (N.A) objective (oil-immersion lens). The spread of incidence angles emanating from the reference sphere of the lens and converging towards the focus includes the resonant angles responsible for SPP excitation at the Ag/air interface, as illustrated in Fig 3.1.

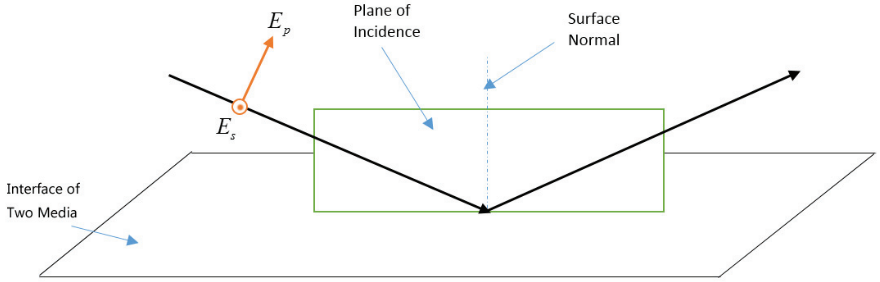

Figure 3.2: The relationship between s-polarization and p-polarization.

Assume a plane wave is incident at the interface of two different materials as illustrated in Fig 3.2. P-polarized light is understood to have an electric field direction parallel to the plane of incidence, and s-polarized light has the electric field oriented

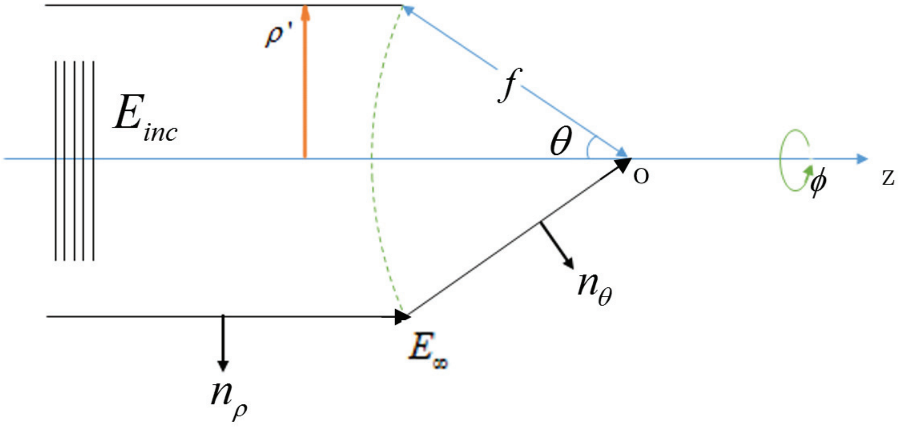

Figure 3.3: Geometrical representation of the focusing process.

perpendicular to that plane. We only consider p-polarization of the incident beam as there is no SPP produced by the s-polarization [39]. In terms of the unit vectors the p-polarized electrical field can be expressed as

$$\mathbf{E}_{inc}^{(p)} = (\mathbf{E}_{inc} \cdot \mathbf{n}_\rho)\mathbf{n}_\rho. \tag{3.1}$$

Here we introduce the unit vectors $\mathbf{n}_\rho$, and $\mathbf{n}_\theta$ as shown in Fig 3.3. As the incident beam is transmitted through the lens, the intensity law must be fulfilled, which means that the energy incident on the aplanatic lens equals the energy leaving the lens . The power carried by a beam of cross-section A equals to $P = (1/2)Z_{\mu\varepsilon}^{-1/2} \int |\mathbf{E}|^2 dA$, where $Z_{\mu\varepsilon} = \sqrt{\mu_0/\varepsilon\varepsilon_0}$ denotes the wave impedance and A is the cross-section area in the plane transverse to the propagation direction [13]. Here μ_0 is the permeability in free space. The field refracts at the spherical surface of the lens and the unit vector $\mathbf{n}_\rho$ is mapped into $\mathbf{n}_\theta$. The refracted electrical field, denoted by $\mathbf{E}_\infty$, to indicate that the field is evaluated at a large distance from the focus $(x, y, z) = (0, 0, 0)$, is expressed as [13]

$$\mathbf{E}_\infty = t^p \left[(\mathbf{E}_{inc} \cdot \mathbf{n}_\rho)\mathbf{n}_\theta\right] \cdot \sqrt{\frac{n_1}{n_2}} (\cos\theta)^{1/2}. \tag{3.2}$$

Here n_1 and n_2 are the refractive indices of the materials on either side of the lens and t^p represents a Fresnel coefficient of the p-polarization [40]. The factor outside the square brackets is due to the energy flux conservation along each ray [13]. Let us assume that the incident TGSM beam is radially polarized such that

$$\mathbf{E}_{inc} = E_{inc}\mathbf{n}_{\rho}. \tag{3.3}$$

The unit vector $\mathbf{n}_{\theta}$ can be expressed in terms of the cylindrical unit vectors $\mathbf{n}_{\rho}$ and $\mathbf{n}_{z}$ using the angle θ. The z-axis is parallel to the incident beam propagation direction as is indicated in Fig 3.3. Thus,

$$\mathbf{n}_{\theta} = \mathbf{n}_{\rho}\cos\theta - \mathbf{n}_{z}\sin\theta. \tag{3.4}$$

Here θ is a convergence angle that a focused ray direction makes with the z-axis. We can then decompose the focused field into radial and axial components as

$$\mathbf{E}_{\infty} = E_{inc}\left[\cos\theta\mathbf{n}_{\rho} - \sin\theta\mathbf{n}_{z}\right](\cos\theta)^{1/2}. \tag{3.5}$$

Here the factor n_1/n_2 is omitted because the two sides of the lens are composed of the same material. The focal length of the lens is much larger than the wavelength of light. Consequently, the field $\mathbf{E}_{\infty}$ on the reference sphere, which can be regarded as far-field, entirely determines the field $\mathbf{E}$ near the focus. According to Eq.(2.17) expressed in the cylindrical coordinates, one can express $\mathbf{E}(\rho,\varphi,z)$ at an arbitrary observation point as

$$\mathbf{E}(\rho,\varphi,z) = \frac{ik_1 f e^{-ik_1 f}}{2\pi}\int_{\theta_\alpha}^{\theta_\beta}\int_{0}^{2\pi}\mathbf{E}_{\infty}e^{ik_1 z\cos\theta}e^{ik_1\rho\sin\theta\cos(\phi-\varphi)}\sin\theta d\phi d\theta. \tag{3.6}$$

Here f is a focal length and the distance r between the focal point and the surface of the sphere was replaced by f. In addition, the integration with respect to θ is confined to the tiny interval $\theta_\alpha \leq \theta \leq \theta_\beta$ to highlight the SPP affect on the transmitted field distributions, where $\theta_\alpha = 42.64°$ and $\theta_\beta = 42.72°$(the simulation configuration corresponds to a $\theta_{spp} = 42.7°$). Further, k_1 and k_3 are wavenumbers in glass and in free space, respectively.

The angular spectrum representation of the transmitted field is given by

$$\mathbf{E}_t(\rho,\varphi,z) = \frac{ik_1 f e^{-ik_1 f}}{2\pi}\int_{\theta_\alpha}^{\theta_\beta}\int_{0}^{2\pi}\mathbf{E}_{\infty}^{t}e^{ik_{3z} z}e^{ik_1\rho\sin\theta\cos(\phi-\varphi)}\sin\theta d\phi d\theta. \tag{3.7}$$

Here $\mathbf{E}_{\infty}^{t}$ is a far-zone expression for the field transmitted through the metal film. It can be determined by applying the appropriate boundary conditions in Eq.(3.5) and is expressed as

$$\mathbf{E}_{\infty}^{t} = \mathbf{E}_{\infty}\widetilde{T}_{13}e^{-ik_{3z}d} = E_{inc}\widetilde{T}_{13}e^{-ik_{3z}d}(\cos\theta)^{1/2}\left[\begin{array}{c}\cos\theta\mathbf{n}_{\rho}\\ -\sin\theta\mathbf{n}_{z}\end{array}\right]. \tag{3.8}$$

The extra factor $e^{-ik_{3z}d}$ ensures that this ratio is properly defined [40]. Here d denotes the thickness of the metal film and $\widetilde{T}_{13}$ is a Fresnel transmission coefficient of the film given by [40]

$$\widetilde{T}_{13} = \frac{t_{23}^{\rho}t_{12}^{\rho}e^{ik_{2z}d}}{1 - r_{21}^{\rho}r_{23}^{\rho}e^{2ik_{2z}d}}, \tag{3.9}$$

where t_{ij}^{p} and r_{ij}^{p} $(i, j = 1, 2, 3)$ are the p-polarization Fresnel transmission and reflection coefficients at each interface of the film. Using Eqs.(3.7) - (3.9), the transmitted field can be decomposed into the radial and axial components with the magnitudes

$$\begin{aligned}
E_{t\rho} &= \frac{ik_1 f e^{-ik_1 f}}{2\pi}\int_{\theta_\alpha}^{\theta_\beta}\int_{0}^{2\pi} E_{inc}\widetilde{T}_{13}e^{-ik_{3z}d}(\cos\theta)^{1/2}e^{ik_{3z}z}e^{ik_1\rho\sin\theta\cos(\phi-\varphi)}\sin\theta\cos\theta d\phi d\theta,\\
E_{tz} &= -\frac{ik_1 f e^{-ik_1 f}}{2\pi}\int_{\theta_\alpha}^{\theta_\beta}\int_{0}^{2\pi} E_{inc}\widetilde{T}_{13}e^{-ik_{3z}d}(\cos\theta)^{1/2}e^{ik_{3z}z}e^{ik_1\rho\sin\theta\cos(\phi-\varphi)}\sin^2\theta d\phi d\theta.
\end{aligned} \tag{3.10}$$

To any statistical optical field, E_{inc} is a fluctuating function of the angular variables and it should be regarded as a random process. Thus, according to the outline of the second-order coherence theory of Chap.2, the cross-spectral density W_{spp} of the electric field on the metal surface can be expressed as

$$W_{spp} = \left\langle E_t^{*}(\rho_1, \varphi_1, z)E_t(\rho_2, \varphi_2, z)\right\rangle. \tag{3.11}$$

Substituting Eq.(3.10) into (3.11), the W_{spp} is represented as

$$
\begin{aligned}
W_{spp} &= \left\langle \frac{k_1^2 f^2}{4\pi^2} \int_{\theta_\alpha}^{\theta_\beta} \int_0^{2\pi} E_{inc}^*(\rho_1,\phi_1) K_1^* d\theta_1 d\phi_1 \int_{\theta_\alpha}^{\theta_\beta} \int_0^{2\pi} E_{inc}(\rho_2,\phi_2) K_2 d\theta_2 d\phi_2 \right\rangle \\
&= \frac{k_1^2 f^2}{4\pi^2} \int_{\theta_\alpha}^{\theta_\beta} \int_0^{2\pi} \int_{\theta_\alpha}^{\theta_\beta} \int_0^{2\pi} \langle E_{inc}^*(\rho_1,\phi_1) E_{inc}(\rho_2,\phi_2) \rangle K_1^* K_2 d\theta_1 d\phi_1 d\theta_2 d\phi_2 \qquad (3.12) \\
&= \frac{k_1^2 f^2}{4\pi^2} \int_{\theta_\alpha}^{\theta_\beta} \int_0^{2\pi} \int_{\theta_\alpha}^{\theta_\beta} \int_0^{2\pi} W_{TGSM}(\rho_1,\phi_1,\rho_2,\phi_2) K_1^* K_2 d\theta_1 d\phi_1 d\theta_2 d\phi_2,
\end{aligned}
$$

Here the functions K_j are defined as

$$
\begin{aligned}
K_j &= \exp[-ik_{3z}d + ik_{3z}z + ik_1\rho\sin\theta_j\cos(\phi_j - \varphi)] \\
&\times \widetilde{T}_{13}(\cos\theta_j)^{\frac{1}{2}} \sin\theta_j \times \begin{cases} \cos\theta_j, & \text{radial factor,} \\ -\sin\theta_j, & \text{axial factor,} \end{cases}
\end{aligned}
\qquad (3.13)
$$

where j=1,2 and items in the square brackets denote the different factors used to calculate radial and axial components of W_{spp}, respectively.

W_{TGSM} in Eq.(3.12) can be regarded as the cross-spectral density of TGSM, as we use a tightly focused twisted Gaussian-Schell model beam to excite SPPs. Recall that the cross-spectral density of TGSM is expressed as

$$
W_{TGSM}(\boldsymbol{\rho}_1,\boldsymbol{\rho}_2) \propto \exp\left(-\frac{\rho_1^2+\rho_2^2}{4\sigma_I^2}\right) \exp\left[-\frac{(\boldsymbol{\rho}_1-\boldsymbol{\rho}_2)^2}{2\sigma_c^2}\right] \exp\left[iu\rho_1\rho_2\sin(\phi_1-\phi_2)\right], \qquad (3.14)
$$

where $\boldsymbol{\rho}_1$, $\boldsymbol{\rho}_2$ as position vectors in the beam cross-section; σ_I and σ_c represent the beam width and the spatial coherence length, respectively, and u stands for the twist parameter.

W_{TGSM} can be expressed in terms of the coherent-mode representation as [18]

$$
W_{TGSM}(\boldsymbol{\rho}_1,\boldsymbol{\rho}_2) = \sum_{m=-\infty}^{\infty} \sum_{n=0}^{\infty} \lambda_{mn} \psi_{mn}^*(\rho_1,\phi_1) \psi_{mn}(\rho_2,\phi_2), \qquad (3.15)
$$

where

$$
\lambda_{mn} = \frac{n!}{(n+|m|)!} \zeta^{n+\frac{|m|}{2}} \eta^m, \qquad (3.16)
$$

and

$$\psi_{mn}(\rho,\phi) = \left(\frac{\rho}{\ell_\perp}\right)^{|m|} L_n^{|m|}\left(\frac{\rho^2}{{\ell_\perp}^2}\right) e^{-\frac{\rho^2}{2{\ell_\perp}^2}} e^{im\varphi}. \tag{3.17}$$

Here $L_n^{|m|}(x)$ is an associate Laguerre polynomial of order n and azimuthal index m; $\ell_\perp$ is a characteristic width of each mode in the transverse plane, given by

$$\ell_\perp = \sqrt{\frac{2\sigma_c^2\sigma_I^2(1+\zeta)}{(2\sigma_I^2+\sigma_c^2)(1-\zeta)}}. \tag{3.18}$$

The factors ζ and η in Eq.(3.16) specify the weight of each mode in the coherent-mode representation of TGSM, through the expressions [18]

$$\frac{1}{2\sigma_I^2} = \frac{1+\zeta-(\eta+1/\eta)\sqrt{\zeta}}{(1-\zeta){\ell_\perp}^2}, \tag{3.19}$$

$$\frac{1}{\sigma_c^2} = \frac{(\eta+1/\eta)\sqrt{\zeta}}{(1-\zeta){\ell_\perp}^2}, \tag{3.20}$$

and

$$u = \frac{(\eta-1/\eta)\sqrt{\zeta}}{(1-\zeta){\ell_\perp}^2}. \tag{3.21}$$

Inverting these equations, the quantities ζ and η can be expressed in terms of the beam parameters. From Eqs.(3.20) and (3.21), the relationship between $u\sigma_c^2$ and η is found to be

$$\eta = \sqrt{\frac{1+u\sigma_c^2}{1-u\sigma_c^2}}. \tag{3.22}$$

Together with the non-negativity of every coefficient λ_{mn} [25], it leads to the constraint on the twist parameter, expressed as

$$-1 \le u\sigma_c^2 \le 1. \tag{3.23}$$

The explicit derivations of modal weights in both maximal twist and no twist cases are given in Appendix A. After substituting from Eqs.(A.10) and (A.12) into Eq.(3.15), the cross-spectral density of a TGSM beam with the maximum twist can be expressed as

$$W_{TGSM}(\boldsymbol{\rho}_1,\boldsymbol{\rho}_2|u\sigma_c^2=1) = \sum_{m=0}^{\infty}\frac{(1+\sigma_c^2/2\sigma_I^2)^{-m}}{m!}\left(\frac{\rho_1\rho_2}{{\ell_\perp}^2}\right)^m e^{-(\rho_1^2+\rho_2^2)/2{\ell_\perp}^2} e^{im(\phi_2-\phi_1)}, \tag{3.24}$$

and the cross-spectral density of a TGSM beam with no twist can be expressed as

$$W_{TGSM}(\boldsymbol{\rho}_1,\boldsymbol{\rho}_2|u\sigma_c^2=0)=\sum_{m=-\infty}^{\infty}\sum_{n=0}^{\infty}\left(1+\frac{\sigma_c^2}{2\sigma_I^2}-\frac{\sigma_c}{\sigma_I}\sqrt{\frac{\sigma_c^2}{4\sigma_I^2}+1}\right)^{n+\frac{|m|}{2}}\frac{n!}{(n+|m|)!}$$
$$\times\left(\frac{\rho_1\rho_2}{{\ell_\perp}^2}\right)^{|m|}L_n^{|m|}\left(\frac{\rho_1^2}{{\ell_\perp}^2}\right)L_n^{|m|}\left(\frac{\rho_2^2}{{\ell_\perp}^2}\right)e^{-(\rho_1^2+\rho_2^2)/2{\ell_\perp}^2}e^{im(\phi_2-\phi_1)}. \tag{3.25}$$

As is seen in Fig.3.3, ρ can be expressed in terms of θ as

$$\rho=f\sin\theta. \tag{3.26}$$

Thus, the cross-spectral densities of TGSM beams can be represented as functions of θ as

$$W_{TGSM}(u\sigma_c^2=1)=\sum_{m=0}^{\infty}\frac{(1+\sigma_c^2/2\sigma_I^2)^{-m}}{m!}\left(\frac{f\sin\theta_1 f\sin\theta_2}{{\ell_\perp}^2}\right)^m \times e^{-(f^2\sin^2\theta_1+f^2\sin^2\theta_2)/2{\ell_\perp}^2}e^{im(\phi_2-\phi_1)}, \tag{3.27}$$

and

$$W_{TGSM}(u\sigma_c^2=0)=\sum_{m=-\infty}^{\infty}\sum_{n=0}^{\infty}\left(1+\frac{\sigma_c^2}{2\sigma_I^2}-\frac{\sigma_c}{\sigma_I}\sqrt{\frac{\sigma_c^2}{4\sigma_I^2}+1}\right)^{n+\frac{|m|}{2}}\frac{n!}{(n+|m|)!}$$
$$\times\left(\frac{f\sin\theta_1 f\sin\theta_2}{{\ell_\perp}^2}\right)^{|m|}L_n^{|m|}\left(\frac{f^2\sin^2\theta_1}{{\ell_\perp}^2}\right)L_n^{|m|}\left(\frac{f^2\sin^2\theta_2}{{\ell_\perp}^2}\right)$$
$$\times e^{-(f^2\sin^2\theta_1+f^2\sin^2\theta_2)/2{\ell_\perp}^2}e^{im(\phi_2-\phi_1)}. \tag{3.28}$$

Further, substituting from Eqs.(3.27) and (3.28) into Eq.(3.12), the expressions for the cross-spectral densities of the electric field near the film with no twist and maximum twist can be written as

$$W_{spp}(\boldsymbol{\rho}_1,\boldsymbol{\rho}_2|u\sigma_c^2=1)=\frac{k_1^2f^2}{4\pi^2}\int_{\theta_\alpha}^{\theta_\beta}\int_0^{2\pi}\int_{\theta_\alpha}^{\theta_\beta}\int_0^{2\pi}\sum_{m=0}^{\infty}\frac{(1+\sigma_c^2/2\sigma_I^2)^{-m}}{m!}\left(\frac{f\sin\theta_1 f\sin\theta_2}{{\ell_\perp}^2}\right)^m$$
$$\times e^{-(f^2\sin^2\theta_1+f^2\sin^2\theta_2)/2{\ell_\perp}^2}e^{im(\phi_2-\phi_1)}K_1^*K_2\,d\theta_1 d\phi_1 d\theta_2 d\phi_2, \tag{3.29}$$

and

$$W_{spp}(\boldsymbol{\rho}_1,\boldsymbol{\rho}_2|u\sigma_c^2=0)=\frac{k_1^2f^2}{4\pi^2}\int\limits_{\theta_\alpha}^{\theta_\beta}\int\limits_{0}^{2\pi}\int\limits_{\theta_\alpha}^{\theta_\beta}\int\limits_{0}^{2\pi}\sum_{m=-\infty}^{\infty}\sum_{n=0}^{\infty}\left(1+\frac{\sigma_c^2}{2\sigma_I^2}-\frac{\sigma_c}{\sigma_I}\sqrt{\frac{\sigma_c^2}{4\sigma_I^2}+1}\right)^{n+\frac{|m|}{2}}$$
$$\times\frac{n!}{(n+|m|)!}\left(\frac{f\sin\theta_1 f\sin\theta_2}{{\ell_\perp}^2}\right)^{|m|}L_n^{|m|}\left(\frac{f^2\sin^2\theta_1}{{\ell_\perp}^2}\right)L_n^{|m|}\left(\frac{f^2\sin^2\theta_2}{{\ell_\perp}^2}\right)$$
$$\times e^{-(f^2\sin^2\theta_1+f^2\sin^2\theta_2)/2{\ell_\perp}^2}e^{im(\phi_2-\phi_1)}K_1^*K_2d\theta_1d\phi_1d\theta_2d\phi_2. \tag{3.30}$$

Extracting the iteration factors, the rest parts of both Eqs.(3.29) and (3.30) can be decomposed into products of two double integrals, which can be calculated respectively. Then Eqs.(3.29) and (3.30) can be written as

$$W_{spp}(\boldsymbol{\rho}_1,\boldsymbol{\rho}_2|u\sigma_c^2=1)=\frac{k_1^2f^2}{4\pi^2}\sum_{m=0}^{\infty}\frac{(1+\sigma_c^2/2\sigma_I^2)^{-m}}{m!}\int\limits_{\theta_\alpha}^{\theta_\beta}\int\limits_{0}^{2\pi}P_1^*d\theta_1d\phi_1\int\limits_{\theta_\alpha}^{\theta_\beta}\int\limits_{0}^{2\pi}P_2d\theta_2d\phi_2, \tag{3.31}$$

and

$$W_{spp}(\boldsymbol{\rho}_1,\boldsymbol{\rho}_2|u\sigma_c^2=0)=\frac{k_1^2f^2}{4\pi^2}\sum_{m=-\infty}^{\infty}\sum_{n=0}^{\infty}\left(1+\frac{\sigma_c^2}{2\sigma_I^2}-\frac{\sigma_c}{\sigma_I}\sqrt{\frac{\sigma_c^2}{4\sigma_I^2}+1}\right)^{n+\frac{|m|}{2}}\frac{n!}{(n+|m|)!}$$
$$\times\int\limits_{\theta_\alpha}^{\theta_\beta}\int\limits_{0}^{2\pi}P_1^*d\theta_1d\phi_1\int\limits_{\theta_\alpha}^{\theta_\beta}\int\limits_{0}^{2\pi}P_2d\theta_2d\phi_2. \tag{3.32}$$

Here P_j is defined as

$$P_j=\left(\frac{f\sin\theta_j}{\ell_\perp}\right)^{|m|}L_n^{|m|}\left(\frac{f^2\sin^2\theta_j}{\ell_\perp^2}\right)e^{-(f^2\sin^2\theta_j)/2\ell_\perp^2}e^{im\phi_j}$$
$$\times e^{-ik_{3z}d+ik_{3z}z+ik_1\rho\sin\theta_j\cos(\phi_j-\varphi)}\widetilde{T}_{13}(\cos\theta_j)^{\frac{1}{2}}\sin\theta_j\times\begin{cases}\cos\theta_j, & \text{radial factor,}\\ -\sin\theta_j, & \text{axial factor,}\end{cases} \tag{3.33}$$

where $j=1,2.$ and P_j differs when calculating different components of W_{spp},

Notice that the Laguerre polynomial $L_n^{|m|}(\frac{f^2sin^2\theta_j}{\ell_\perp^2})$ equals to 1 in the maximal twist case because $n=0$.

Thus Eqs.(3.31) and (3.32) give us the cross-spectral densities of SPP-enhanced fields in both no twist and maximal twist cases.

Now let us consider the angular momentum density $\mathbf{L}$ of the fields near the interface. The average angular momentum density $\mathbf{L}$ is defined as [41]

$$< \mathbf{L} >=< \boldsymbol{\rho} \times \mathbf{S} >, \tag{3.34}$$

where $\boldsymbol{\rho}$ represents the in-plain position vector and $\mathbf{S}$ denotes the Poynting vector, defined as $\mathbf{S} = \mathbf{E} \times \mathbf{H}$, where $\mathbf{H}$ is the magnetic field. One of the Maxwell equations in free space takes the form

$$\nabla \times \mathbf{E}(\mathbf{r}, t) = -\mu_0 \frac{\partial \mathbf{H}(\mathbf{r}, t)}{\partial t}, \tag{3.35}$$

in the space-time domain and

$$\nabla \times \mathbf{E}(\mathbf{r}, \omega) = -i\mu_0 \omega \mathbf{H}(\mathbf{r}, \omega), \tag{3.36}$$

in the space-frequency domain. Thus the magnetic field $\mathbf{H}$ can be expressed as

$$\mathbf{H} = -(i\omega\mu_0)^{-1}(\nabla \times \mathbf{E}). \tag{3.37}$$

Further, the magnetic fields near the film needs to be derived to obtain the explicit expression of angular momentum density of the SPP-enhanced fields. There is no azimuthal component of $\mathbf{E}_t$, implying that $\mathbf{E}_{t\varphi} = 0$. Recall Eq.(3.10) that the transmitted electrical field $\mathbf{E}_t$ can be decomposed into the radial and axial components with the magnitudes $E_{t\rho}$ and E_{tz}. Applying Eq.(3.37) into Eq.(3.7), each component of the magnetic field $\mathbf{H}$ in the cylindrical coordinates can be expressed in terms of the electric field components as

$$\begin{aligned} \mathbf{H}_\rho &= -(\omega\mu_0)^{-1}[k_1 \sin\theta \sin(\phi - \varphi) E_{tz}]\mathbf{n}_\rho, \\ \mathbf{H}_\varphi &= -(\omega\mu_0)^{-1}[k_{3z} E_{t\rho} - k_1 \sin\theta \cos(\phi - \varphi) E_{tz}]\mathbf{n}_\varphi, \\ \mathbf{H}_z &= (\omega\mu_0)^{-1}[k_1 \sin\theta \sin(\phi - \varphi) E_{t\rho}]\mathbf{n}_z. \end{aligned} \tag{3.38}$$

The average magnitudes of Poynting vector components can be derived from Eqs.(3.7) and (3.38) as

$$\begin{aligned}
S_\rho &= -\left\langle E_{tz}(\theta_1,\phi_1)H^*_\varphi(\theta_2,\phi_2)\right\rangle = (\omega\mu_0)^{-1}[k_{3z}\left\langle E^*_{t\rho}E_{tz}\right\rangle - k_1\sin\theta_2\cos\left(\phi_2-\varphi\right)\langle E^*_{tz}E_{tz}\rangle],\\
S_\varphi &= \left\langle E_{tz}(\theta_1,\phi_1)H^*_\rho(\theta_2,\phi_2) - E_{t\rho}(\theta_1,\phi_1)H^*_z(\theta_2,\phi_2)\right\rangle\\
&= -(\omega\mu_0)^{-1}[k_1\sin\theta_2\sin(\phi_2-\varphi)](\langle E^*_{tz}E_{tz}\rangle + \left\langle E^*_{t\rho}E_{t\rho}\right\rangle),\\
S_z &= \left\langle E_{t\rho}(\theta_1,\phi_1)H^*_\varphi(\theta_2,\phi_2)\right\rangle = -(\omega\mu_0)^{-1}[k_{3z}\left\langle E^*_{t\rho}E_{t\rho}\right\rangle - k_1\sin\theta_2\cos\left(\phi_2-\varphi\right)\langle E^*_{tz}E_{t\rho}\rangle].
\end{aligned} \tag{3.39}$$

Notice that the factors $\left\langle E^*_{t\rho}E_{tz}\right\rangle$, $\langle E^*_{tz}E_{tz}\rangle$, $\left\langle E^*_{t\rho}E_{t\rho}\right\rangle$ and $\langle E^*_{tz}E_{t\rho}\rangle$ can be represented in terms of W_{TGSM} using Eqs.(3.10), (3.12) and (3.13). Here we define $K_{j\rho}$ and K_{jz} developed from Eq.(3.13) to denote the option of K_j to calculate either of radial and axial components, repectively, such that

$$\begin{aligned}
K_{j\rho} &= \exp[-ik_{3z}d + ik_{3z}z + ik_1\rho\sin\theta_j\cos(\phi_j-\varphi)]\widetilde{T}_{13}(\cos\theta_j)^{\frac{1}{2}}\sin\theta_j\cos\theta_j,\\
K_{jz} &= -\exp[-ik_{3z}d + ik_{3z}z + ik_1\rho\sin\theta_j\cos(\phi_j-\varphi)]\widetilde{T}_{13}(\cos\theta_j)^{\frac{1}{2}}\sin^2\theta_j,
\end{aligned} \tag{3.40}$$

where $j = 1, 2$.

Thus, substituting Eqs.(3.10) - (3.12) into (3.39), the Poynting vector components can be expressed in terms of Eq.(3.40), respectively,

$$\begin{aligned}
S_\rho =& \frac{k_1^2 f^2}{4\pi^2\omega\mu_0}[\int_{\theta_\alpha}^{\theta_\beta}\int_0^{2\pi}\int_{\theta_\alpha}^{\theta_\beta}\int_0^{2\pi} k_{3z}W_{TGSM}K^*_{2\rho}K_{1z}d\theta_1 d\phi_1 d\theta_2 d\phi_2\\
&-\int_{\theta_\alpha}^{\theta_\beta}\int_0^{2\pi}\int_{\theta_\alpha}^{\theta_\beta}\int_0^{2\pi} k_1\sin\theta_2\cos\left(\phi_2-\varphi\right)W_{TGSM}K^*_{2z}K_{1z}d\theta_1 d\phi_1 d\theta_2 d\phi_2],
\end{aligned} \tag{3.41}$$

$$\begin{aligned}
S_\varphi =& -\frac{k_1^2 f^2}{4\pi^2\omega\mu_0}[\int_{\theta_\alpha}^{\theta_\beta}\int_0^{2\pi}\int_{\theta_\alpha}^{\theta_\beta}\int_0^{2\pi} k_1\sin(\phi_2-\varphi)\sin\theta_2 W_{TGSM}K^*_{2z}K_{1z}d\theta_1 d\phi_1 d\theta_2 d\phi_2\\
&+\int_{\theta_\alpha}^{\theta_\beta}\int_0^{2\pi}\int_{\theta_\alpha}^{\theta_\beta}\int_0^{2\pi} k_1\sin(\phi_2-\varphi)\sin\theta_2 W_{TGSM}K^*_{2\rho}K_{1\rho}d\theta_1 d\phi_1 d\theta_2 d\phi_2],
\end{aligned} \tag{3.42}$$

and

$$\begin{aligned}
S_z =& -\frac{k_1^2 f^2}{4\pi^2\omega\mu_0}[\int_{\theta_\alpha}^{\theta_\beta}\int_0^{2\pi}\int_{\theta_\alpha}^{\theta_\beta}\int_0^{2\pi} k_{3z}W_{TGSM}K^*_{2\rho}K_{1\rho}d\theta_1 d\phi_1 d\theta_2 d\phi_2\\
&-\int_{\theta_\alpha}^{\theta_\beta}\int_0^{2\pi}\int_{\theta_\alpha}^{\theta_\beta}\int_0^{2\pi} k_1\sin\theta_2\cos\left(\phi_2-\varphi\right)W_{TGSM}K^*_{2z}K_{1\rho}d\theta_1 d\phi_1 d\theta_2 d\phi_2].
\end{aligned} \tag{3.43}$$

Using the coherent-mode representation of W_{TGSM} expressed in Eqs.(3.27) and (3.28), the expressions of Poynting vectors of the transmitted fields can be decomposed into combinations of double integrals, similar to the derivation of W_{spp}. Thus, Eqs.(3.41) - (3.43) can be transformed into

$$\begin{aligned} S_\rho = B[&\int_{\theta_\alpha}^{\theta_\beta}\int_0^{2\pi} P_{1z} d\theta_1 d\phi_1 \int_{\theta_\alpha}^{\theta_\beta}\int_0^{2\pi} k_{3z} P_{2\rho}^* d\theta_2 d\phi_2 \\ &- \int_{\theta_\alpha}^{\theta_\beta}\int_0^{2\pi} P_{1z} d\theta_1 d\phi_1 \int_{\theta_\alpha}^{\theta_\beta}\int_0^{2\pi} k_1 \sin\theta_2 \cos(\phi_2-\varphi) P_{2z}^* d\theta_2 d\phi_2], \end{aligned} \tag{3.44}$$

$$\begin{aligned} S_\varphi = -B[&\int_{\theta_\alpha}^{\theta_\beta}\int_0^{2\pi} P_{1z} d\theta_1 d\phi_1 \int_{\theta_\alpha}^{\theta_\beta}\int_0^{2\pi} k_1 \sin\theta_2 \sin(\phi_2-\varphi) P_{2z}^* d\theta_2 d\phi_2 \\ &+ \int_{\theta_\alpha}^{\theta_\beta}\int_0^{2\pi} P_{1\rho} d\theta_1 d\phi_1 \int_{\theta_\alpha}^{\theta_\beta}\int_0^{2\pi} k_1 \sin\theta_2 \sin(\phi_2-\varphi) P_{2\rho}^* d\theta_2 d\phi_2], \end{aligned} \tag{3.45}$$

and

$$\begin{aligned} S_z = -\,B[&\int_{\theta_\alpha}^{\theta_\beta}\int_0^{2\pi} P_{1\rho} d\theta_1 d\phi_1 \int_{\theta_\alpha}^{\theta_\beta}\int_0^{2\pi} k_{3z} P_{2\rho}^* d\theta_2 d\phi_2 \\ &- \int_{\theta_\alpha}^{\theta_\beta}\int_0^{2\pi} P_{1\rho} d\theta_1 d\phi_1 \int_{\theta_\alpha}^{\theta_\beta}\int_0^{2\pi} k_1 \sin\theta_2 \cos(\phi_2-\varphi) P_{2z}^* d\theta_2 d\phi_2], \end{aligned} \tag{3.46}$$

where the parameters $P_{j\rho}$ and P_{jz} are factors developed from Eq.(3.33), expressed as

$$\begin{aligned} P_{j\rho} &= \left(\frac{f\sin\theta_j}{\ell_\perp}\right)^{|m|} L_n^{|m|}\left(\frac{f^2\sin^2\theta_j}{\ell_\perp^2}\right) e^{-(f^2\sin^2\theta_j)/2\ell_\perp^2} e^{im\phi_j} \\ &\times e^{-ik_{3z}d+ik_{3z}z+ik_1\rho\sin\theta_j\cos(\phi_j-\varphi)} \widetilde{T}_{13}(\cos\theta_j)^{\frac{3}{2}} \sin\theta_j, \\ P_{jz} &= -\left(\frac{f\sin\theta_j}{\ell_\perp}\right)^{|m|} L_n^{|m|}\left(\frac{f^2\sin^2\theta_j}{\ell_\perp^2}\right) e^{-(f^2\sin^2\theta_j)/2\ell_\perp^2} e^{im\phi_j} \\ &\times e^{-ik_{3z}d+ik_{3z}z+ik_1\rho\sin\theta_j\cos(\phi_j-\varphi)} \widetilde{T}_{13}(\cos\theta_j)^{\frac{1}{2}} \sin^2\theta_j, \end{aligned} \tag{3.47}$$

and B is defined as

$$B(u\sigma_c = 1) = \frac{k_1^2 f^2}{4\pi^2 \omega \mu_0} \sum_{m=0}^{\infty} \frac{(1+\sigma_c^2/2\sigma_I^2)^{-m}}{m!}, \tag{3.48}$$

for the maximal twist case and as

$$B(u\sigma_c = 0) = \frac{k_1^2 f^2}{4\pi^2 \omega \mu_0} \sum_{m=-\infty}^{\infty} \sum_{n=0}^{\infty} \left(1 + \frac{\sigma_c^2}{2\sigma_I^2} - \frac{\sigma_c}{\sigma_I}\sqrt{\frac{\sigma_c^2}{4\sigma_I^2} + 1}\right)^{n+\frac{|m|}{2}} \frac{n!}{(n+|m|)!}, \tag{3.49}$$

for the incident beams with no twist.

As a result, the expressions for nonzero components of the angular momentum density **L** are obtained using Eqs.(3.44) - (3.46) as

$$< \mathbf{L}_\varphi >= -\rho S_z \mathbf{n}_\varphi, \tag{3.50}$$

and

$$< \mathbf{L}_z >= \rho S_\varphi \mathbf{n}_z. \tag{3.51}$$

3.2 Results

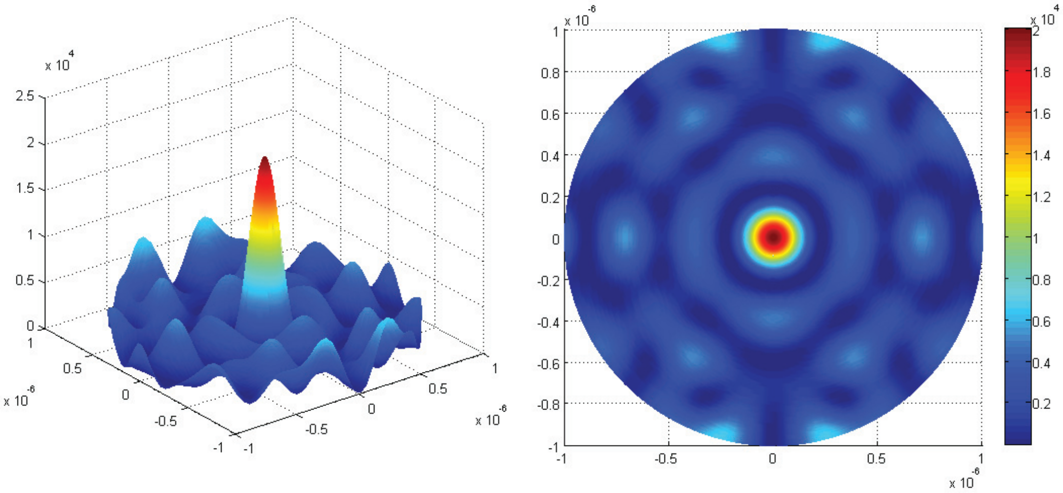

Figure 3.4: Optical intensity in the glass-silver-air configuration.

In our numerical simulations, we excite SPPs on a 50nm thick silver film, corresponding to an SPP coupling angle $\theta_{spp} = \pm 42.7°$ with a tightly focused, radially polarized twisted Gaussian-Schell model beam. The wavelength of the beam equals to 632nm. The integration domain is confined to a tiny angular area to stress a strong

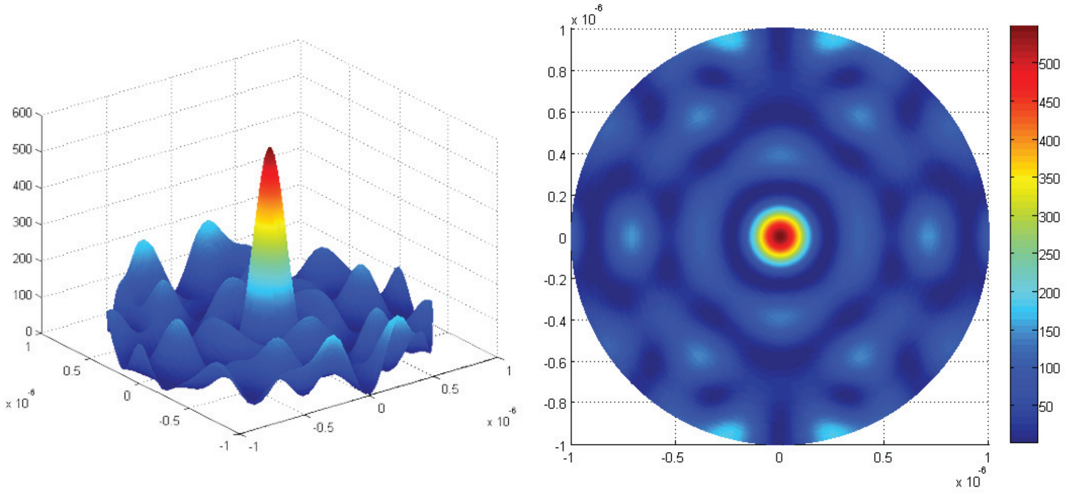

Figure 3.5: Optical intensity in the glass-air configuration.

impact of SPPs. Thus we choose a lens with N.A.=1.4 to make sure the angular spread exceeds θ_{spp}. The relative permittivities are $\varepsilon_1 = 2.3$, $\varepsilon_2 = -18.3 + 0.5i$ and $\varepsilon_3 = 1$, corresponding to glass, silver and air, respectively.

Fig 3.4 shows the simulation results for the cross-spectral density W_{spp} on the silver surface parallel to the air-silver interface and having dimensions of 2 $\mu m \times 2\mu m$. The main peak of the optical intensity is centered at the optical axis, which is shown in the figure. The results prove that the SPPs propagate from the axis toward the periphery of the focal plane. To verify the SPP enhancement, we remove a silver film from the configuration and present the resulting intensity distribution in Fig 3.5. Compared with Figure 3.4, the distribution of intensity in Fig.3.5 shows quite similar properties. However, the maximum intensity is reduced by a factor of 30 in the absence of SPPs. In addition, Figs.3.4 and 3.5 verify our original assumption that strong plasmon coupling can be realized in the Kretschmann configuration.

The components of the average angular momentum density $< \mathbf{L} >$ of the transmitted fields near the film are calculated as well. Fig.3.6 shows the azimuthal components of $< \mathbf{L} >$ for input beams of different coherence states in the no twist case. It can be seen in the figure that as the coherence length σ_c decreases, the incident beam switches from the nearly coherent state to a nearly incoherent state. As a result, the sharp angular momentum maxima and their periodic distribution tend to be smeared out.

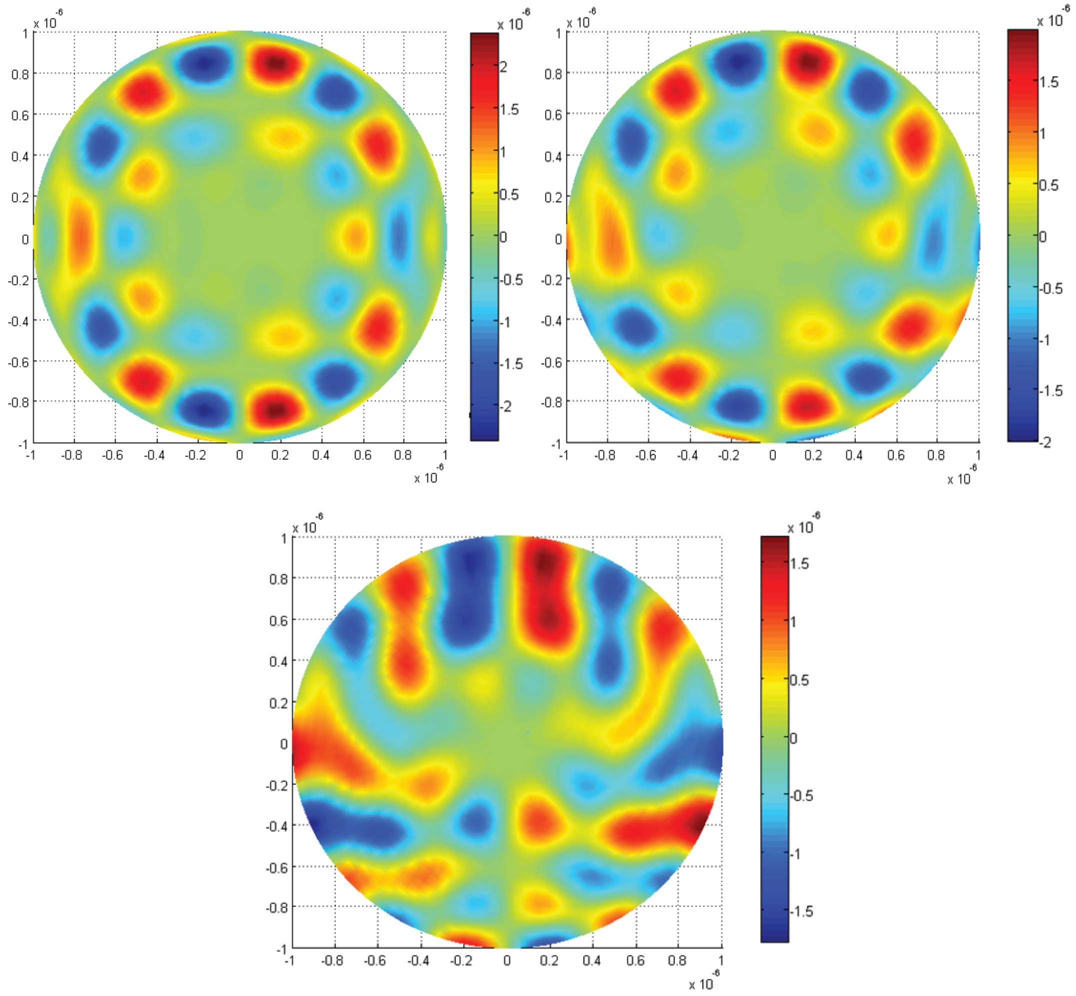

Figure 3.6: Azimuthal component of the averaged angular momentum density in no twist condition with (a)$\sigma_c = 10^5\sigma_I$, (b)$\sigma_c = \sigma_I$, (c)$\sigma_c = 0.5\sigma_I$.

In addition, the distribution and periodicity of the angular momentum density can be controlled by adjusting the magnitude of the twist parameter. These results are shown in Fig.3.7 and Fig.3.8 where the axial components of $< \mathbf{L} >$ are displayed in both maximal twist and no twist cases with the same coherence length $\sigma_c = 0.5\sigma_I$. Compared with the no twist case, the effective region of angular momentum density in the maximal twist is much larger. Nevertheless, the magnitude of angular momentum density declines obviously. It can be understood that the rotating energy of the beam has been delocalized by employing twist effect into the incident beam. This result can be applied in the optical microparticle manipulation, such as the optical

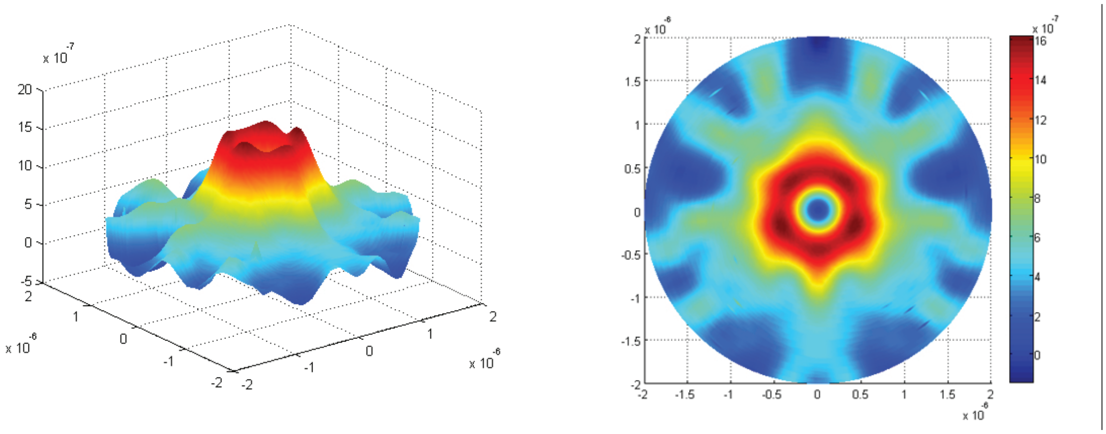

Figure 3.7: Axial component of the angular momentum density with $u\sigma_c^2 = 1$ and coherence length $\sigma_c = 0.5\sigma_I$.

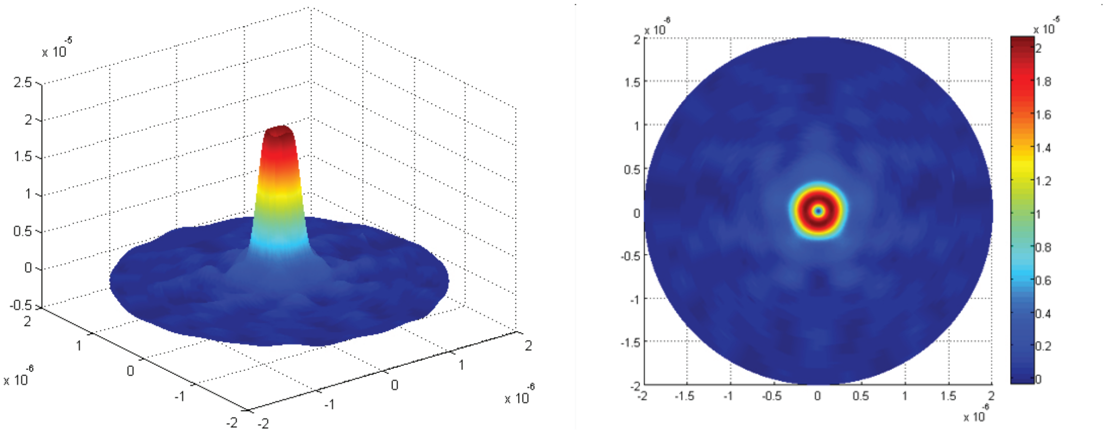

Figure 3.8: Axial component of the angular momentum density with $u = 0$ and coherence length $\sigma_c = 0.5\sigma_I$.

tweezer technology, which is a well-known tool in numerous fields of biology, chemistry and physics [42]. Using this technology, particles may be trapped or moved along certain trajectory at the focal plane of a microscopes objective according to the field distribution of applied beam [43] and the rotation velocity of optical vortex is controlled by the orbital angular momentum carried by the beam. A typical configuration of trapping system is shown in Fig.(3.9). By controlling the twist phase of the incident light, the distribution of angular momentum density will variate between the no twist and maximal twist cases. Thus, the results can be used to set parameters of the trapping system, such as the optical torques and the operating area. Another potential application of this result is to obtain a well-defined beam shape with a randomly-diffused intensity profile by the amplitude of twist phase, as the similar function of homogenizer. Yet another potential application of our results is to the generation of non-spreading partially coherent spatio-temporal beams, optical bullets, in the plasmonics context [44].

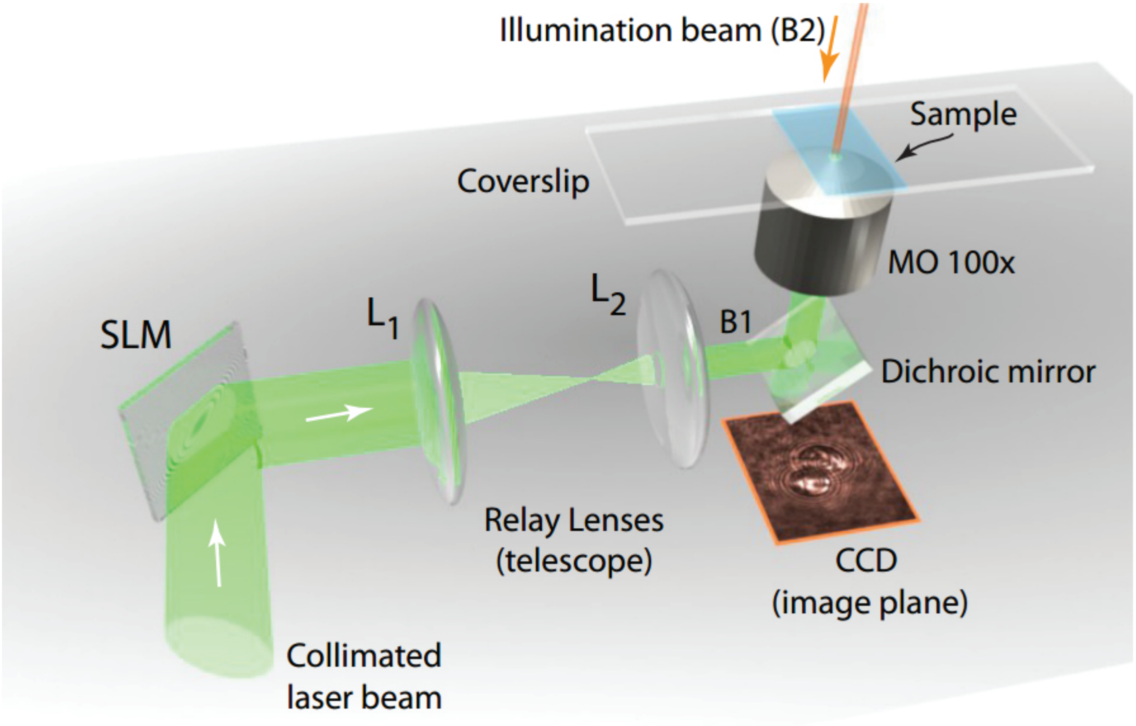

Figure 3.9: Configuration of a holographic optical trapping system(Figure source: [43]).

Chapter 4

Conclusions and Future Work

4.1 Conclusions

In this thesis, we use partially coherent, twisted Gaussian-Schell model beams focused by a lens to excite SPPs on a thin silver film. The properties of SPP-enhanced transmitted beams are examined by adjusting the parameters affecting coherence, including the coherence length of the beams and the twist parameter. The simulation uses the so-called Kretschmann configuration, which is a convenient configuration to be realized experimentally.

To derive the SPP-enhanced angular momentum density distribution of light, several mathematical tools have been applied, including the angular spectrum representation, coherent-mode representation and far-fields transformation. The cross-spectral density of in-coupled light has been simulated and shows reasonable properties. It is strongly affected by the SPP generation, proving that the Kretschmann configuration can produce SPPs. In addition, most of the incident beam energy is coupled into SPPs.

The results of simulations indicate an opportunity to control the angular momentum density distribution by adjusting the beam coherence length and the magnitude of its twist phase. Potential applications are related to the areas of optical tweezers [45, 46], higher dimensional classical and quantum communications [47, 48] and microscopy [49] .

4.2 Recommendations for future work

Although the results presented here have demonstrated the intensity and angular momentum density distribution control by adjusting the degree of coherence phase, the work can be further extended in several aspects.

First of all, the results are based on numerical simulations, which means that the experimental validation is required. Furthermore, the incident beams applied in our simulations have radial polarization. Finally, we can use other types of incident polarization at the source plane, such as azimuthal and linear polarizations.

Bibliography

[1] B. Mahon. *The man who changed everything: the life of James Clerk Maxwell.* John Wiley & Sons, 2004.

[2] W. K. Miner and R. Markoll. A double-blind trial of the clinical effects of pulsed electromagnetic fields in osteoarthritis. *J rheumatol*, 20:456–460, 1993.

[3] M. Kawasaki and T. Moroi. Electromagnetic cascade in the early universe and its application to the big-bang nucleosynthesis. *arXiv preprint astro-ph/9412055*, 1994.

[4] X. Che, I. Wells, G. Dickers, P. Kear, and X. Gong. Re-evaluation of rf electromagnetic communication in underwater sensor networks. *Communications Magazine, IEEE*, 48(12):143–151, 2010.

[5] L. Wang, F. Che, S. A. Ponomarenko, and Z. Chen. Plasmon-enhanced spectral changes in surface sum-frequency generation with polychromatic light. *Optics express*, 21(12):14159–14168, 2013.

[6] E. Stefan and B. Nicolas. *Plasmonics: From Basics to Advanced Topics.* Springer, 2012.

[7] S. A. Maier. *Plasmonics: fundamentals and applications: fundamentals and applications.* Springer Science & Business Media, 2007.

[8] Y. Xia and N. J. Halas. Shape-controlled synthesis and surface plasmonic properties of metallic nanostructures. *MRS bulletin*, 30(05):338–348, 2005.

[9] D. Chang, A. S. Sørensen, P. Hemmer, and M. Lukin. Quantum optics with surface plasmons. *Physical review letters*, 97(5):053002, 2006.

[10] A. Hartschuh, E. J. Sánchez, S. Xie, and L. Novotny. High-resolution near-field raman microscopy of single-walled carbon nanotubes. *Physical Review Letters*, 90(9):095503, 2003.

[11] M. E. Stewart, C. R. Anderton, L. B. Thompson, J. Maria, S. K. Gray, J. A. Rogers, and R. G. Nuzzo. Nanostructured plasmonic sensors. *Chemical reviews*, 108(2):494–521, 2008.

[12] M. Kauranen and A. V. Zayats. Nonlinear plasmonics. *Nature Photonics*, 6(11):737–748, 2012.

[13] L. Novotny and B. Hecht. *Principles of nano-optics.* Cambridge university press, 2012.

[14] M. C. Teich and B. Saleh. *Fundamentals of photonics*. 1991.

[15] H. Kano, S. Mizuguchi, and S. Kawata. Excitation of surface-plasmon polaritons by a focused laser beam. *JOSA B*, 15(4):1381–1386, 1998.

[16] A. Bouhelier, F. Ignatovich, A. Bruyant, C. Huang, G. Colas, J. Weeber, A. Dereux, G. P. Wiederrecht, and L. Novotny. Surface plasmon interference excited by tightly focused laser beams. *Optics letters*, 32(17):2535–2537, 2007.

[17] J. W. Goodman. *Statistical optics*, volume 1. Wiley-Interscience, 1985.

[18] S. A. Ponomarenko. Twisted gaussian schell-model solitons. *Physical Review E*, 64(3):036618, 2001.

[19] R. Ritchie. Plasma losses by fast electrons in thin films. *Physical Review*, 106(5):874, 1957.

[20] C. Clemmow. *The Plane Wave Spectrum Representation of Electromagnetic Fields: International Series of Monographs in Electromagnetic Waves*. Elsevier, 2013.

[21] A. B. Shvartsburg and A. A. Maradudin. *Waves in gradient metamaterials*. World Scientific, 2013.

[22] M. Janda. Digital hologram synthesis. Technical report, Technical Report DCSE/TR-2007-02, University of West Bohemia, 2007.

[23] O. Korotkova and G. Gbur. Angular spectrum representation for propagation of random electromagnetic beams in a turbulent atmosphere. *JOSA A*, 24(9):2728–2736, 2007.

[24] R. E. Hummel. *Optische Eigenschaften von Metallen und Legierungen*. Springer, 1971.

[25] A. S. Ostrovsky. Coherent-mode representations in optics. SPIE, 2006.

[26] B. E. Saleh. Intensity distribution due to a partially coherent field and the collett-wolf equivalence theorem in the fresnel zone. *Optics Communications*, 30(2):135–138, 1979.

[27] F. Gori. Collett-wolf sources and multimode lasers. *Optics Communications*, 34(3):301–305, 1980.

[28] Y. Cai, Q. Lin, and O. Korotkova. Ghost imaging with twisted gaussian schell-model beam. *Optics express*, 17(4):2453–2464, 2009.

[29] C. Wen, C. Lim, A. Ye, and J. J. Zhu. Single-molecule force measurement via optical tweezers reveals different kinetic features of two braf mutants responsible for cardio-facial-cutaneous (cfc) syndrome. *Biomedical optics express*, 4(12):2835–2845, 2013.

[30] K. Carlsson, P. Danielsson, A. Liljeborg, L. Majlöf, R. Lenz, and N. Åslund. Three-dimensional microscopy using a confocal laser scanning microscope. *Optics letters*, 10(2):53–55, 1985.

[31] S. Kawata and Y. Kawata. Three-dimensional optical data storage using photochromic materials. *Chemical Reviews*, 100(5):1777–1788, 2000.

[32] K. Greulich, G. Pilarczyk, A. Hoffmann, G. Meyer, Z. H.örste, B. Schäfer, V. Uhl, and S. Monajembashi. Micromanipulation by laser microbeam and optical tweezers: from plant cells to single molecules. *Journal of microscopy*, 198(3):182–187, 2000.

[33] O. Maragò, R. Saija, F. Borghese, P. Denti, P. Jones, E. Messina, G. Compagnini, V. Amendola, M. Meneghetti, M. Iatì, et al. Plasmon-enhanced optical trapping of metal nanoparticles: force calculations and light-driven rotations of nanoaggregates. In *SPIE NanoScience+ Engineering*, page 77622. International Society for Optics and Photonics, 2010.

[34] M. Padgett and L. Allen. Light with a twist in its tail. *Contemporary Physics*, 41(5):275–285, 2000.

[35] D. L. Marks, B. J. Davis, S. A. Boppart, and P. S. Carney. Partially coherent illumination in full-field interferometric synthetic aperture microscopy. *JOSA A*, 26(2):376–386, 2009.

[36] E. Verhagen, L. Kuipers, and A. Polman. Field enhancement in metallic subwavelength aperture arrays probed by erbium upconversion luminescence. *Optics express*, 17(17):14586–14598, 2009.

[37] E. Ozbay. Plasmonics: merging photonics and electronics at nanoscale dimensions. *science*, 311(5758):189–193, 2006.

[38] H. A. Atwater. The promise of plasmonics. *Scientific American*, 296(4):56–62, 2007.

[39] T. Hatano, B. Nishikawa, H. Kurosawa, and T. Ishihara. Transverse photo voltage induced by circularly polarized light in metallic photonic crystal slabs. In *Quantum Electronics and Laser Science Conference*, page 5. Optical Society of America, 2008.

[40] W. C. Chew. *Waves and fields in inhomogeneous media*, volume 522. IEEE press New York, 1995.

[41] C. Schulze, A. Dudley, R. Brüning, M. Duparré, and A. Forbes. Measurement of the orbital angular momentum density of bessel beams by projection into a laguerre–gaussian basis. *Applied optics*, 53(26):5924–5933, 2014.

[42] A. Ashkin. Optical trapping and manipulation of neutral particles using lasers. *Proceedings of the National Academy of Sciences*, 94(10):4853–4860, 1997.

[43] J. Rodrigo, A. Caravaca-Aguirre, T. Alieva, G. Cristóbal, M. Calvo, et al. Microparticle movements in optical funnels and pods. *Optics Express*, 19:5232–5243, 2011.

[44] S. A. Ponomarenko and G. P. Agrawal. Linear optical bullets. *Optics Communications*, 261:1–4, 2006.

[45] J. E. Curtis, B. A. Koss, and D. G. Grier. Dynamic holographic optical tweezers. *Optics Communications*, 207(1):169–175, 2002.

[46] M. K. Kreysing, T. Kießling, A. Fritsch, C. Dietrich, J. R. Guck, and J. A. Käs. The optical cell rotator. *Optics Express*, 16(21):16984–16992, 2008.

[47] G. Gibson, J. Courtial, M. Padgett, M. Vasnetsov, V. Pas' ko, S. Barnett, and S. Franke-Arnold. Free-space information transfer using light beams carrying orbital angular momentum. *Optics Express*, 12(22):5448–5456, 2004.

[48] A. Vaziri, G. Weihs, and A. Zeilinger. Experimental two-photon, three-dimensional entanglement for quantum communication. *Physical Review Letters*, 89(24):240401, 2002.

[49] S. W. Hell and J. Wichmann. Breaking the diffraction resolution limit by stimulated emission: stimulated-emission-depletion fluorescence microscopy. *Optics letters*, 19(11):780–782, 1994.

[50] S. A. Ponomarenko and E. Wolf. Universal structure of field correlations within a fluctuating medium. *Physical Review E*, 65(1):016602, 2001.

Appendix A

Modal Weights in the Maximal Twist and No Twist Cases

We can use beam parameters σ_I and σ_c to determine ζ. By combining Eqs.(3.19) and (3.20), it follows that

$$\frac{\sigma_c^2}{2\sigma_I^2} = \frac{1+\zeta-(\eta+1/\eta)\sqrt{\zeta}}{(\eta+1/\eta)\sqrt{\zeta}}. \tag{A.1}$$

Thus

$$\left(1+\frac{\sigma_c^2}{2\sigma_I^2}\right)\frac{\eta^2+1}{\eta}\sqrt{\zeta} = 1+\zeta. \tag{A.2}$$

Since η can be expressed in terms of u and σ_c, it can be derived that

$$\eta^2+1 = \frac{2}{1-\sigma_c^2}. \tag{A.3}$$

On substituting from Eq.(A.3) into (A.2), it follows that

$$2\left(1+\frac{\sigma_c^2}{2\sigma_I^2}\right)\sqrt{\zeta} = (1+\zeta)\eta(1-u\sigma_c^2). \tag{A.4}$$

On substituting from Eq.(3.22) into (A.4), we obtain a quadratic equation for ζ as

$$\zeta\sqrt{1-u^2\sigma_c^4} - 2(1+\sigma_c^2/2\sigma_I^2)\sqrt{\zeta} + \sqrt{1-u^2\sigma_c^4} = 0. \tag{A.5}$$

The solution to Eq.(A.5) reads

$$\sqrt{\zeta} = \frac{(1+\sigma_c^2/2\sigma_I^2) \pm \sqrt{(1+\sigma_c^2/2\sigma_I^2)^2-(1-u^2\sigma_c^4)}}{\sqrt{1-u^2\sigma_c^4}}. \tag{A.6}$$

If $u\sigma_c^2 = 1$, the right-hand side of Eq.(A.6) approaches infinity with the plus sign. Thus solution of Eq.(A.6) makes sense with the minus sign and ζ is expressed as

$$\zeta = \frac{[(1+\sigma_c^2/2\sigma_I^2) - \sqrt{(1+\sigma_c^2/2\sigma_I^2)^2-(1-u^2\sigma_c^4)}]^2}{1-u^2\sigma_c^4}. \tag{A.7}$$

It follows from Eq.(A.7) that

$$\zeta = \frac{[(1+\sigma_c^2/2\sigma_I^2) - (1+\sigma_c^2/2\sigma_I^2)\sqrt{1-\frac{(1-u^2\sigma_c^4)}{(1+\sigma_c^2/2\sigma_I^2)^2}}]^2}{1-u^2\sigma_c^4},$$

implying that in the limit $u\sigma_c^2 \to 1$,one can expand the right-hand side into a Taylor series resulting in the approximation

$$\zeta \simeq \frac{[(1+\sigma_c^2/2\sigma_I^2) - (1+\sigma_c^2/2\sigma_I^2) + (1+\sigma_c^2/2\sigma_I^2)\frac{1-u^2\sigma_c^4}{2(1+\sigma_c^2/2\sigma_I^2))^2}]^2}{1-u^2\sigma_c^4},$$

or

$$\zeta \simeq \frac{1-u^2\sigma_c^4}{4(1+\sigma_c^2/2\sigma_I^2)^2}. \tag{A.8}$$

Now we will consider two limiting situations: $u\sigma_c^2 = 0$ (no twist) and $u\sigma_c^2 = 1$ (maximal twist).

When $u\sigma_c^2 = 1$, η and ζ are found to satisfy the limiting conditions including

$$\eta = \sqrt{\frac{2}{1-u\sigma_c^2}} \to \infty,$$

$$\sqrt{\zeta} = \frac{\sqrt{1-u^2\sigma_c^4}}{2(1+\sigma_c^2/2\sigma_I^2)} \to 0,$$

and

$$\eta\sqrt{\zeta} = \sqrt{\frac{2}{1-u\sigma_c^2}}\frac{\sqrt{(1+u\sigma_c^2)(1-u\sigma_c^2)}}{2(1+\sigma_c^2/2\sigma_I^2)} = \frac{1}{\sqrt{2}(1+\sigma_c^2/2\sigma_I^2)} < \infty.$$

Recall the expression for λ_{mn} in (3.16). It can be shown that when $m \leq 0$, $\lambda_{mn} \to 0$. On the other hand, when $m > 0$, Eq.(3.16) implies in this limit that

$$\lambda_{mn} = \frac{n!}{(n+|m|)!}\zeta^n(\eta\sqrt{\zeta})^m \to 0 \qquad \text{unless} \qquad n = 0. \tag{A.9}$$

Thus only the modes with the azimuthal index $n = 0$ contribute to the field density in the maximal twist case such that

$$\lambda_{mn} = \begin{cases} \frac{\delta_{n0}}{m!}(1+\sigma_c^2/2\sigma_I^2)^{-m}, & m > 0; \\ 0, & m \leq 0. \end{cases} \tag{A.10}$$

Here δ_{n0} is the Kronecker delta symbol, defined as

$$\delta_{n0} = \begin{cases} 1, & n = 0; \\ 0, & n \neq 0. \end{cases} \tag{A.11}$$

Similarly, the amplitudes of η and ζ in the no twist case can be found from Eqs.(A.6) to (A.10) as

$$\eta = 1,$$

and

$$\zeta = \left(1 + \frac{\sigma_c^2}{2\sigma_I^2} - \frac{\sigma_c}{\sigma_I}\sqrt{\frac{\sigma_c^2}{4\sigma_I^2} + 1}\right)^2 .$$

Thus in this case, λ_{mn} can be expressed as

$$\lambda_{mn} = \left(1 + \frac{\sigma_c^2}{2\sigma_I^2} - \frac{\sigma_c}{\sigma_I}\sqrt{\frac{\sigma_c^2}{4\sigma_I^2} + 1}\right)^{n + \frac{|m|}{2}} \frac{n!}{(n + |m|)!}. \tag{A.12}$$

Appendix B

Numerical Codes for Solving Spectral Density

```
%*********************************************************************
%Numerical Codes for Solving Spectral Density excited by focused TGSM
   beam
%*********************************************************************
%
% Program author: Hao Cheng
% Department of Electrical and Computer Engineering
% Dalhousie University
% 1360 Barrington St.
% Halifax, NS B3J 2X4
% 902-999-7218
% hz427921@dal.ca
%
% Date of this version: Mar.28 2015
%
%*********************************************************************
clear all
clc
%%%parameters
ee1=2.3;                                  %permittivity of glass
ee2=-18.3+0.51i;                          %permittivity of silver
ee3=1.0;                                  %permittivity of air
n1=sqrt(ee1);                             %refractive index of glass
n2=sqrt(ee2);                             %refractive index of silver
n3=ee3;                                   %refractive index of air
ee=8.8542e-12;                            %permittivity in free space
uu=1.2566e-6;                             %permeability in free space
cc=2.99792458e8;                          %speed of light
i=sqrt(-1);
f=1e-3;                                   %focal length
```

```
d=50e-9;                                %thickness of silver
wavelength=632e-9;
taoc=94;                                %coherence length
taoi=94e-5;                             %beam width
w=2*pi*cc/wavelength;
z=f+d;
k=w/cc;                             %wavenumber in free space
k1=k*n1;
k2=k*n2;
k3=k*n3;
ltrans=sqrt(1/(1/taoc^2+1/(2*taoi^2)));
%%%equation
syms theta Fi ffi p m
k1z=k1*cos(theta);
k2z=sqrt(k2^2-(k1*sin(theta))^2);
k3z=sqrt(k3^2-(k1*sin(theta))^2);
t23=2*ee3*k2z*sqrt(ee2/ee3)/(ee3*k2z+ee2*k3z);
r23=(ee3*k2z-ee2*k3z)/(ee3*k2z+ee2*k3z);
t13=2*ee3*k1z*sqrt(ee1/ee3)/(ee3*k1z+ee1*k3z);
t12=2*ee2*k1z*sqrt(ee1/ee2)/(ee2*k1z+ee1*k2z);
r21=(ee1*k2z-ee2*k1z)/(ee1*k2z+ee2*k1z);
T13=t23*t12*exp(i*k2z*d)/(1-r21*r23*exp(2*i*k2z*d));      %Fresnel
    coefficient
kernal1=cos(theta)*(f*sin(theta)/ltrans)^(m)*exp(-(f*sin(theta))^2/(2*
    ltrans^2))*(cos(theta))^0.5*sin(theta);
kernal2=exp(i*m*Fi-i*k3z*d+i*k3z*(z-f)+i*k1*p*sin(theta)*cos(Fi-ffi))*
    abs(T13)/k1z;
part1=kernal1*kernal2;
%loop to calculate spectral density on each point in domain
pp=linspace(0,1e-6,100);
fifi=linspace(0,2*pi,100);
for l=1:length(pp)
      p1=pp(l)
     for j=1:length(fifi)
         f1=fifi(j)
         x(l,j) = p1.*cos(f1);
         y (l,j)= p1.*sin(f1);
         C=0;
          for mm=0:3
```

```
          kernalfinal1=inline(subs(part1,{p,ffi,m},{p1,f1,mm}),'theta','Fi');
          A=dblquad(kernalfinal1,0,0.2373*pi,0,2*pi);
          %%part outside of integral
          thegema=k1^2*f^2/(4*pi^2)*(1+taoc^2/((2*taoi)^2))^(-mm)/factorial(mm);
           C(mm+1)=A*A'*thegema;
          end
          zz(l,j)=sum(C(:));
    end
    save('wpp_u1_big','x','y','zz');
end
```

Appendix C

Numerical Codes for Solving Angular Momentum Density

```
%**********************************************************************
%Numerical Codes for Solving Angular Momentum Density excited by focused
    TGSM beam
%**********************************************************************
%
% Program author: Hao Cheng
% Department of Electrical and Computer Engineering
% Dalhousie University
% 1360 Barrington St.
% Halifax, NS B3J 2X4
% 902-999-7218
% hz427921@dal.ca
%
% Date of this version: Mar.28 2015
%
%**********************************************************************
clear all
clc
%%%parameters
ee1=2.3;                          %permittivity of glass
ee2=-18.3+0.51i;                  %permittivity of silver
ee3=1.0;                          %permittivity of air
n1=sqrt(ee1);                     %refractive index of glass
n2=sqrt(ee2);                     %refractive index of silver
n3=ee3;                           %refractive index of air
ee=8.8542e-12;                    %permittivity in free space
uu=1.2566e-6;                     %permeability in free space
cc=2.99792458e8;                  %speed of light
i=sqrt(-1);
f=1e-3;                           %focal length
```

```
d=50e-9;
wavelength=632e-9;
taoc=94;
taoi=94e-5;
w=2*pi*cc/wavelength;
z=f+d;
k=w/cc;
k1=k*n1;
k2=k*n2;
k3=k*n3;
ltrans=sqrt(1/(1/taoc^2+1/(2*taoi^2)));
%%%equations
syms theta Fi ffi p m
k1z=k1*cos(theta);
k2z=sqrt(k2^2-(k1*sin(theta))^2);
k3z=sqrt(k3^2-(k1*sin(theta))^2);
t23=2*ee3*k2z*sqrt(ee2/ee3)/(ee3*k2z+ee2*k3z);
r23=(ee3*k2z-ee2*k3z)/(ee3*k2z+ee2*k3z);
t13=2*ee3*k1z*sqrt(ee1/ee3)/(ee3*k1z+ee1*k3z);
t12=2*ee2*k1z*sqrt(ee1/ee2)/(ee2*k1z+ee1*k2z);
r21=(ee1*k2z-ee2*k1z)/(ee1*k2z+ee2*k1z);
T13=t23*t12*exp(i*k2z*d)/(1-r21*r23*exp(2*i*k2z*d));
part1z=-sin(theta)*(f*sin(theta)/ltrans)^(m)*exp(-(f*sin(theta))^2/(2*
    ltrans^2))*(cos(theta))^1.5*sin(theta);
part1p=cos(theta)*(f*sin(theta)/ltrans)^(m)*exp(-(f*sin(theta))^2/(2*
    ltrans^2))*(cos(theta))^1.5*sin(theta);
part2=exp(i*m*Fi-i*k3z*d+i*k3z*(z-f)+i*k1*p*sin(theta)*cos(Fi-ffi))*abs(
    T13)/k1z;
A=part1p*part2;
B=part1p*(part2*k3z);
C=part1z*part2*k1*sin(theta)*cos(Fi-ffi);
%%integral
pp=linspace(0,1e-6,100);
fifi=linspace(0,2*pi,100);
for l=1:length(pp)
      p1=pp(l)
    for j=1:length(fifi)
         f1=fifi(j)
         x(l,j) = p1.*cos(f1);
```

```
         y (l,j)= p1.*sin(f1);
         X=0;
          for mm=0:2
          kernalfinalA=inline(subs(A,{p,ffi,m},{p1,f1,mm}),'theta','Fi')
             ;
          kernalfinalB=inline(subs(B',{p,ffi,m},{p1,f1,mm}),'theta','Fi'
             );
          kernalfinalC=inline(subs(C',{p,ffi,m},{p1,f1,mm}),'theta','Fi'
             );
          A1=dblquad(kernalfinalA,0.2369*pi,0.2373*pi,0,2*pi);
          B1=dblquad(kernalfinalB,0.2369*pi,0.2373*pi,0,2*pi);
          C1=dblquad(kernalfinalC,0.2369*pi,0.2373*pi,0,2*pi);
          %part outside of integral
          thegema=k1^4*f^2/(4*pi^2)/w/uu*(1+taoc^2/((2*taoi)^2))^(-mm)/
             factorial(mm);
           X(mm+1)=((A1)*((B1)-(C1)))*thegema;
          end
          zz(l,j)=sum(X(:));
    end
    save('Sz_u1_big','x','y','zz');
end
```